

MEASUREMENTS OF FISSION PRODUCT  
SORPTION ON GRAPHITE

---

A Dissertation

presented to

the Faculty of the Graduate School

at the University of Missouri-Columbia

---

In Partial Fulfillment

of the Requirements for the Degree

Doctor of Philosophy

---

by

JOHN-DAVID BERNARD-LUDWIG-PHILIP SEELIG

Tushar K. Ghosh, Dissertation Co-Supervisor

Sudarshan K. Loyalka, Dissertation Co-Supervisor

MAY 2017

© Copyright by John-David Seelig 2017

All Rights Reserved

The undersigned, appointed by the Dean of the Graduate School, have examined the dissertation entitled

MEASUREMENTS OF FISSION PRODUCT SORPTION ON GRAPHITE

presented by John-David Seelig

candidate for the degree of doctor of philosophy

And hereby certify that, in their opinion, it is worthy of acceptance.

---

TUSHAR K. GHOSH

---

SUDARSHAN K. LOYALKA

---

ROBERT V. TOMPSON

---

MARK A. PRELAS

---

C. MICHAEL GREENLIEF

---

JOHN D. BROCKMAN

## ACKNOWLEDGMENTS

The work performed was possible only through the guidance and help of the faculty and staff of the Nuclear Science and Engineering Institute at the University of Missouri (MU). Additionally, great benefit was obtained through the use of highly sophisticated facilities. Their full use was possible through the assistance and guidance of mentors, professors, supervisors, assistants and staff of the College of Engineering and College of Chemistry at MU, the University of Missouri Research Reactor Center, and the NASA Glenn Research Center. My sincere gratitude goes to Drs. Tushar Ghosh, Sudarshan Loyalka, John Brockman, Luke Carter, Nathan Jacobson, Michael Greenlief, Robert Tompson, and Mark Prelas.

I am thankful for all the funding that made my work possible. This includes a U.S. Department of Energy grant funded by the Nuclear Energy University Programs (NEUP-2982), entitled “A Research Program on FP and Dust Transport in HTGRs.” I am also thankful for the support of a GAANN grant from the U.S. Department of Education and a grant from the U.S. Nuclear Regulatory Commission. I am grateful to Dr. Dietmar Kobertz (of Forschungszentrum Jülich GmbH) for sharing his detailed sample preparation and measurement methods. Special thanks are due NASA GRC for hosting me and giving me the opportunity to participate in collaborative work and to use their KEMS facilities. I am thankful for the additional technical and theoretical support from Dr. Gustavo Costas, Judy Auping and Pete Bonacuse. I am also grateful to Amir Ashivai and Brandon Radoman-Shaw at Case Western Reserve University for the use of their highly-specialized SEM device at the SCSAM Case School of Engineering.

# TABLE OF CONTENTS

ACKNOWLEDGMENTS .....	ii
LIST OF FIGURES .....	vi
LIST OF TABLES .....	viii
LIST OF ABBREVIATIONS.....	ix
NOMENCLATURE .....	x
ABSTRACT.....	xii
Chapter 1. Introduction.....	1
1.1. Background.....	1
1.2. Objectives .....	5
Chapter 2. Review of Previous Work.....	7
2.1. Adsorption.....	7
2.2. Fission Product Isotherms.....	10
2.3. Technique and Previous Results .....	13
Chapter 3. Instrumentation and Material Preparation .....	24
3.1. Knudsen Effusion Mass Spectrometry.....	24
3.1.1. Introduction .....	24
3.1.2. Knudsen Cell Effusion.....	25
3.1.3. Auxiliary Equipment .....	28
3.1.4. Mass Analyzers.....	31

3.2.	Sample Preparation .....	35
3.2.1.	Graphite Powder .....	35
3.2.2.	Metal Nitrate Decomposition .....	36
3.2.3.	Instrumental Neutron Activation Analysis .....	36
3.2.4.	Scanning Electron Microscopy and Energy Dispersive X-ray Spectroscopy	38
Chapter 4.	Methods for Calibration and Data Acquisition and Analysis .....	39
4.1.	Spectrometry Analysis .....	39
4.2.	Equilibrium Points .....	44
4.3.	KEMS Calibrations .....	46
4.4.	Preliminary Strontium Results .....	48
4.5.	Solid Phase Mass Estimation .....	51
Chapter 5.	Results .....	54
5.1.	Sample Characterization .....	54
5.1.1.	Concentrations .....	54
5.1.2.	Qualitative Imaging .....	56
5.2.	KEMS Experiments .....	62
5.2.1.	Calibration Results .....	62
5.2.2.	Strontium .....	64
5.2.3.	Silver .....	66
Chapter 6.	Discussion and Future Work .....	70
6.1.	Discussion of Data Quality .....	70

6.2.	Silver Isotherm Fit .....	73
6.3.	Importance of Data .....	75
6.4.	Other Areas of Future Work .....	77
	References .....	79
	Appendix 1: Additional Reference Theory .....	84
a)	Equilibrium Constant Relation .....	84
b)	Thermodynamic Generalization .....	84
c)	Neutron Activation Analysis (NAA) .....	85
d)	Mass–Weight Calibration .....	86
	Appendix 2: Supplemental Raw Data .....	87
a)	KEMS Raw Data Samples .....	87
b)	Shutter Experiments .....	87
c)	Raw Data of First Point .....	88
	Appendix 3: Supplemental Data of Previous Work .....	90
	Appendix 4: Isotherm Regression Material .....	92
a)	Full Ag data .....	92
	VITA .....	93

## LIST OF FIGURES

<b>1</b>	High temperature gas cooled reactor radionuclide retention system.....	<b>2</b>
<b>2</b>	Cesium desorption from various graphite or fuel related materials.....	<b>20</b>
<b>3</b>	Strontium desorption from various graphite or fuel related materials.....	<b>21</b>
<b>4</b>	Cs sorption isotherms from experiments (Exp.) performed (averaging H-451, A3-3 and H-327) and DFT modeling (Graph).....	<b>22</b>
<b>5</b>	Knudsen Effusion mass spectrometer apparatus at Glenn research facility.....	<b>25</b>
<b>6</b>	Sample image of a Knudsen cell.....	<b>26</b>
<b>7</b>	One of the sample configurations Hilpert, Gerads, and Kobertz considered in performing their experiments.....	<b>29</b>
<b>8</b>	Graphic of the effusing species pressure and temperature characterizing the type of mass spectrometry.....	<b>26</b>
<b>9</b>	Shaker and sieves used to separate out the graphite powder.....	<b>35</b>
<b>10</b>	Figure of an experiment performed on 08-04-2015 and involved melting of silver in an alumina cell.....	<b>41</b>
<b>11</b>	Visual raw output from Merlin™ software used at NASA-GRC.....	<b>44</b>
<b>12</b>	Diagram showing the results of the melting phase of the calibration experiment.....	<b>46</b>
<b>13</b>	Data points are similar to Table 10. $\Delta T$ is incorporated to fit the curve to Heat of Vaporization data over this temperature range.....	<b>47</b>
<b>14</b>	The third run of sample 10 shows that drift is still present.....	<b>48</b>
<b>15</b>	Collection of data points for Sr 10 run 3.....	<b>49</b>
<b>16</b>	A log scale plot of the intensity counts of Ag sample 4.....	<b>50</b>
<b>17</b>	IG-110 with strontium present in sample number 10.....	<b>58</b>
<b>18</b>	Enlarged portion of the center particle (Sr sample 10) to illustrate the general size.....	<b>58</b>
<b>19</b>	Energy dispersive X-ray spectroscopy sample of strontium imaged before, but with targeting of the dark areas of the sample.....	<b>58</b>
<b>20</b>	Energy dispersive X-ray spectroscopy data taken at a brighter spot in the sample, particularly a zoomed in feature associated with Figure 18.....	<b>58</b>
<b>21</b>	Energy dispersive X-ray spectroscopy post heating Sr sample 10 run.....	<b>59</b>
<b>22</b>	Energy dispersive X-ray spectroscopy Ag sample 4 before Knudsen effusion mass spectrometry experiment.....	<b>60</b>
<b>23</b>	Energy dispersive X-ray spectroscopy Ag sample 4 after Knudsen effusion mass spectrometry .....	<b>60</b>
<b>24</b>	Scanning Electron Microscope image of Ag (sample 6) on IG-110 graphite taken using back scattering electron filter before Knudsen effusion mass spectrometry experiment.....	<b>61</b>
<b>25</b>	Scanning Electron Microscope image of Ag (sample 6) on IG-110 graphite taken using back scattering electron filter after Knudsen effusion mass spectrometry experiment.....	<b>61</b>

<b>26</b>	AG (Sample 6) in IG-110 post Knudsen effusion mass spectroscopy, using secondary electron imaging.....	<b>62</b>
<b>27</b>	Energy dispersive X-ray spectroscopy of Ag (sample 6) in IG-110 post analysis based on Figure 11.....	<b>62</b>
<b>28</b>	The Ag-IG-110 isotherms given by temperature range: 1100K to 1260K.....	<b>68</b>
<b>29</b>	Enthalpy of vaporizations for Ag in IG-110 graphite by concentration.....	<b>70</b>
<b>A2.1</b>	The thermocouple reading for a Ag calibration sample experiment.....	<b>88</b>
<b>A2.2</b>	Ag in Alumina calibration experiment.....	<b>89</b>
<b>A2.3</b>	Thermocouple reading graph for preliminary Sr on IG-110 experiment.....	<b>90</b>
<b>A2.4</b>	Continuing the analysis from Figure A2.3, this graph shows how pseudo-equilibrium can be achieved.....	<b>90</b>
<b>A3.1</b>	Myers and Bell, enthalpies of vaporization of Sr on H-273 graphite.....	<b>92</b>
<b>A4.1</b>	Ag data including high and low concentration data.....	<b>93</b>

## LIST OF TABLES

<b>1</b>	Interactions of fission products both in-core and ex-core.....	<b>3</b>
<b>2</b>	Experimental table summary of objectives.....	<b>6</b>
<b>3</b>	Summary of some experimental systems used to study adsorption.....	<b>8</b>
<b>4</b>	Sorption parameters for strontium in various graphite and materials.....	<b>16</b>
<b>5</b>	Sorption parameters for cesium in various graphite and materials.....	<b>17</b>
<b>6</b>	Study of H-451 irradiated versus unirradiated of Cesium sorption.....	<b>18</b>
<b>7</b>	Results of nitrogen BET data yielding surface area and pore volume.....	<b>35</b>
<b>8</b>	Table of nuclear reaction from neutron activation and key measurement information regarding gamma ray analysis for INAA.....	<b>37</b>
<b>9</b>	Table of nuclear reaction from neutron activation, and key measurement information regarding gamma ray analysis for INAA.....	<b>37</b>
<b>10</b>	Data from calibration run number 2 using Ag melted in an alumina ceramic cell (Al <sub>2</sub> O <sub>3</sub> ).....	<b>45</b>
<b>11</b>	Loss of silver calculated through Eq. 10 in micrograms per hour.....	<b>51</b>
<b>12</b>	Loss of silver calculated through Eq. 10 in nano-moles per hour.....	<b>51</b>
<b>13</b>	Strontium mass measurements before and after the experiment.....	<b>52</b>
<b>14</b>	Silver Ag measurements before and after the experiment.....	<b>52</b>
<b>15</b>	Concentrations of Sr and Ag samples created for Knudsen effusion mass spectroscopy.....	<b>56</b>
<b>16</b>	Summary of calibrations performed using Ag in Al <sub>2</sub> O <sub>3</sub> cell.....	<b>63</b>
<b>17</b>	Calibration list for sample number concentration.....	<b>64</b>
<b>18</b>	Concentration, Temperature, Pressure data for Sr adsorption to IG-110.....	<b>65</b>
<b>19</b>	Enthalpy of vaporization for Sr on IG-110 as measured by our Knudsen effusion mass spectrometry experiments.....	<b>65</b>
<b>20</b>	Hilpert et al.'s experiments on A3-3 graphite, enthalpy of vaporization for Sr.	<b>66</b>
<b>21</b>	Concentration, Temperature, Pressure data for Ag adsorption to IG-110.....	<b>67</b>
<b>22</b>	Enthalpies of vaporization for Ag on IG-110 as performed at NASA GRC.....	<b>69</b>
<b>23</b>	Results of initial fit to Eq. 33.....	<b>74</b>
<b>24</b>	Results of fit to Eq. 33, but with the fixing of some constants (con).....	<b>75</b>
<b>25</b>	Results of fit to Eq. 34.....	<b>75</b>
<b>A3.1</b>	Review of experimental and modeled binding energy or enthalpy of vaporization of fission product sorbate to designated surface material, or bonding location on a graphene sheet.....	<b>91, 92</b>

## LIST OF ABBREVIATIONS

VHTR	Very High Temperature Reactors
HTGR	High Temperature Gas Cooled Reactors
VHT-GCR	Very High Temperature Gas Cooled Reactors
FP(s)	Fission Product(s)
KEMS	Knudsen Effusion Mass Spectrometry
INAA	Instrumental Neutron Activation Analysis
NGNP	Next Generation Nuclear Plant
NRC	Nuclear Regulatory Commission
DOE	Department of Energy
INL	Idaho National Lab
TRISO	Tristructural-Isotropic
PBR	Pebble Bed Reactors
DFT	Density Functional Theory
VASP	Vienna Ab initio Simulation Package (computer program)
NEUP	Nuclear Energy University Program
Exp.	experimental as indicated
PLATO	Package for Linear-combination of Atomic Orbitals
K-cell	Knudsen Cell
MS	Mass Spectrometry
EI	Electron Ionization
NASA	National Aeronautics and Space Agency
TOF	Time of Flight
Quad	Quadrupole
QMA	Quadrupole Mass Analyzer
BET	Brunauer-Emmett-Teller
MURR	University of Missouri Research Reactor
SEM	Scanning Electron Microscopy
EDS	Energy Dispersive X-ray Spectroscopy
SCSAM	Swagelok Center for Surface Analysis of Materials
STD	Standard Deviation
ITS	International Temperature Scale
FTIR	Fourier Transform Infrared Spectroscopy
BSE	Back-scattered electron imaging
CTP	Concentration – Temperature – Pressure

## NOMENCLATURE

<i>Ag</i>	<i>silver</i>
<i>Sr</i>	<i>strontium</i>
<i>Cs</i>	<i>cesium</i>
<i>C, c</i>	<i>concentration</i>
<i>C<sub>g</sub></i>	<i>surface concentration</i>
<i>C<sub>t</sub></i>	<i>transition constant for surface phase concentration</i>
<i>d<sub>1</sub>, d<sub>2</sub></i>	<i>transition concentration parameters. d<sub>2</sub> has units of 1/Temperature</i>
<i>P, p</i>	<i>pressure</i>
<i>T</i>	<i>temperature</i>
<i>R</i>	<i>ideal gas constant</i>
<b><math>\Delta H'</math></b>	<i>enthalpy per mole</i>
<i>A, B, D, E</i>	<i>constants of integration and coefficients of integration for isotherm equations</i>
<b><math>P_F</math></b>	<i>pressure based on Freundlich Isotherm Equation</i>
<b><math>P_H</math></b>	<i>pressure based on Henrian Isotherm Equation</i>
<i>H-327; A3-3; H-451; P3JHAN</i>	<i>graphite types</i>
<i>K</i>	<i>unit of temperature, Kelvin</i>
<i>mol</i>	<i>mole</i>
<i>m</i>	<i>milli, 10<sup>-3</sup></i>
<i>kg</i>	<i>kilogram</i>
<i>atm</i>	<i>unit of pressure, atmosphere</i>
$\mu$	<i>micro, 10<sup>-6</sup></i>
$\sigma^2$	<i>variance, square of standard deviation, uncertainty</i>
<i>H</i>	<i>as subscript, Henrian</i>
<i>F</i>	<i>as subscript, Freundlich</i>
<i>sp<sup>2</sup>, sp<sup>3</sup></i>	<i>orbital shell hybridizations</i>
<i>NBG-18, IG-110</i>	<i>types of graphite</i>
<i>Pa</i>	<i>unit of pressure, Pascal</i>
$p_A^E$	<i>equilibrium pressure of species (A)</i>
$N_A$	<i>Avogadro's number 6.022 x 10<sup>23</sup></i>
$\tilde{V}$	<i>specific volume</i>
$\pi$	<i>number Pi, 3.14159</i>
$\bar{s}_A$	<i>average molecular speed</i>
$M_A$	<i>molecular weight of species A</i>
<i>Kn</i>	<i>Knudsen number</i>
$\lambda$	<i>mean free path</i>
$r_0$	<i>radius of orifice in K-cell</i>
<i>d</i>	<i>diameter</i>
$A_0$	<i>area of orifice in K-cell</i>
$W_C$	<i>clausing factor</i>
<i>t</i>	<i>time</i>
$n_A$	<i>mass of A</i>

$Torr$	<i>unit of pressure</i>
$F_B$	<i>magnetic force</i>
$Z$	<i>electric charge</i>
$v$	<i>velocity</i>
$B$	<i>magnetic field</i>
$F_C$	<i>centripetal force</i>
$r$	<i>radius</i>
$m_A$	<i>mass of species A</i>
$x,y,z$	<i>unit directions, geometry</i>
$V$	<i>voltage, electric field strength</i>
$\omega$	<i>angular magnetic field strength</i>
$e$	<i>unit electron voltage</i>
$q$	<i>charge, in directions</i>
$u,v$	<i>velocity in x and y directions respectively</i>
$\Phi_0$	<i>total applied electric field strength</i>
$l$	<i>liter</i>
$s$	<i>second</i>
$\sigma$	<i>capture cross section</i>
$I$	<i>intensity</i>
$k$	<i>calibration constant</i>
$\dot{m}_A$	<i>mass rate</i>
$\Delta H_{vap}$	<i>heat of vaporization, enthalpy of vaporization</i>
$\gamma$	<i>branching factor</i>
$\bar{I}_A$	<i>mean intensity</i>
$m$	<i>as subscript, measured</i>
$lit$	<i>as subscript, literature</i>
$obs$	<i>as subscript, observed</i>
$\%E$	<i>error %</i>
$\Delta H$	<i>enthalpy general, in context - heat of vaporization, sorption</i>
$R^2$	<i>statistical measure</i>
$\beta$	<i>lumped constant</i>
$\overline{I(\tau)}$	<i>intensity measured, part of integrand</i>
$\theta$	<i>differential time</i>
$K_p$	<i>equilibrium pressure constant</i>
$g$	<i>as subscript, gas phase</i>
$s$	<i>as subscript, solid phase</i>

$$\int_{\tau}^{\tau+\Delta t} I(t) dt$$

# MEASUREMENTS OF FISSION PRODUCT SORPTION ON GRAPHITE

John-David Bernard-Ludwig-Philip Seelig

Dr. Tushar K. Ghosh, Dissertation Co-Supervisor

Dr. Sudarshan K. Loyalka, Dissertation Co-Supervisor

## **ABSTRACT**

Nuclear source estimations for high and very high gas temperature reactors (VHTRs) require data for fission product (FP) adsorption on graphite at high temperatures. The adsorption and vapor pressures of silver on nuclear moderator grade IG-110 graphite were measured in the range of 1000-1400K. Knudsen Effusion Mass Spectrometry (KEMS) was used for vapor pressure measurements, and Instrumental Neutron Activation Analysis (INAA) was used for measurements of silver adsorbed on graphite. From the data, adsorption isotherms and the enthalpies of vaporization were deduced, and are reported.

## CHAPTER 1. INTRODUCTION

This section discusses the importance of the research work and objectives of the research. The current state of nuclear regulations and reactor safety analysis for the coming generation of nuclear reactors is also discussed.

### **1.1. Background**

The Next Generation Nuclear Plant (NGNP) will be a Nuclear Regulatory Commission (NRC)-licensed commercial high-temperature gas-cooled reactor (HTGR), also known as a very-high temperature reactor (VHTR) plant (prismatic or pebble bed), capable of producing electricity and high temperature process heat [1, 2]. The US Department of Energy (DOE) position on the NRC approval for HTGR licensing was described in the Idaho National Laboratory (INL) Mechanistic Source Terms White Paper, INL/EXT-10-17997, July 2010, and will follow 10 CFR 52 [3]. HTGRs have five barriers to fission product release: the tristructural-isotropic (TRISO) fuel coating, the fuel elements, the core graphite, the primary coolant system, and the reactor building. TRISO fuel can come in two forms, pebbles and hexagonal bricks. The pebble-based macro structure is inherent to the proposed pebble bed reactors (PBRs), and the hexagonal brick orientation is referred to as a prismatic structure [1]. Figure 1 is from the Idaho National Laboratory (INL) 2010 white paper [1 p 13] and shows paths to the source term for a prismatic TRISO fuel HTGR. Similar paths apply to the pebble bed reactors, except for dust because of abrasion. The radionuclides of main interest are

tritium, noble gases, halogens ( $^{131}\text{I}$ ), alkali metals, tellurium group metals, alkaline earth metals, and noble metals [1].

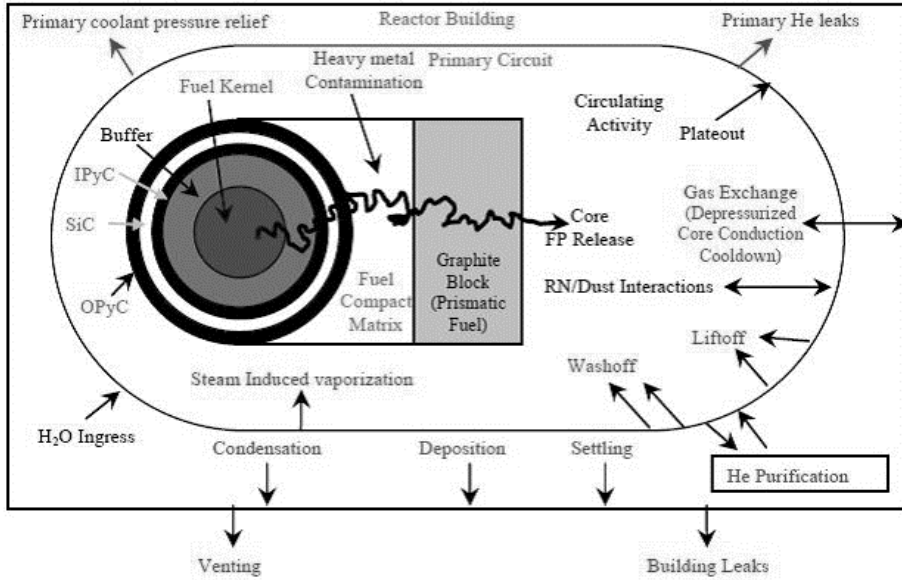


**Figure 1:** HTGR radionuclide retention system [1].

Computational models aim to study the first four retentive barriers for normal conditions, as well as to address the factors that lead to the releases, and contribute to the source terms during accident conditions. Table 1 describes some interactions of various fission products (FPs) both in-core and ex-core [1].

The INL white paper [1] emphasizes the need for new data and computations for the final barrier to release: FP diffusion and adsorption and interactions with dust. As an example, the white paper comments,

“The quantities and form of dust in current designs for HTGRs are unknown. . .” [1 p 44]

Correlations are needed that give the sorptivities of these nuclides as a function of temperature, partial pressure, surface state, and coolant chemistry for normal operating and accident conditions.” [1 p 48]

**Table 1:** Interactions of fission products both in-core and ex-core. Excerpt is from Walton et al. [4] on a review of iodine and other fission product sorption for gas cooled VHTRs.

<b>Radionuclide Class</b>	<b>Key Nuclide</b>	<b>Form in Fuel</b>	<b>Principal In-Core Behavior</b>	<b>Principal Ex-Core Behavior</b>
Tritium	$^3\text{H}$	Gas	Permeates intact SiC; sorbs on core graphite	Permeates through heat exchangers
Noble gases	$^{133}\text{Xe}$	Gas	Retained by PyC/SiC	Removed by helium purification system
Halogens	$^{131}\text{I}$	Gas	Retained by PyC/SiC	Deposits on colder metals
Alkali metals	$^{137}\text{Cs}$	Oxide-element	Retained by SiC; some matrix/graphite retention	Deposits on metals/dust
Tellurium group	$^{132}\text{Te}$	Complex	Retained by PyC/SiC	Deposits on metals/dust
Alkaline earths	$^{90}\text{Sr}$	Oxide-carbide	High matrix/graphite retention	Deposits on metals/dust
Noble metals	$^{110\text{m}}\text{Ag}$	Elemental	Permeates intact SiC	Deposits on metals

Graphite has been chosen as the structural and containment material for nuclear fuel; thus, it is a significant component of HTGRs and VHTRs. These reactors can achieve thermal efficiencies of approximately 50%, which is much greater than current power reactors, which is roughly 36% [5]. To increase handling safety the fuel will be self-contained in the graphite structure, a TRISO orientation [1].

Graphite's inherent porosity has the advantage of enabling a direct gaseous cooling system, as proposed in the very high temperature gas cooled reactors (VHT-GCR) design [1, 6]. Operating reactors typically aim to extend their fuel life cycles by adding boric acid as an extra moderator [2]. While this prolongs the fuel, it can and has damaged the cooling system. VHTRs bypass this need as graphite porosity allows gaseous cooling systems and absorbs fission products in its interstitial spaces. Although the retention rate is of interest because it becomes possible for fission products to escape the TRISO fuel

coating shell and travel into the graphite. Two primary mechanisms are associated with this kind of transport: diffusion and kinetics [1, 7].

Given that graphite will contain fission products it is important to understand if these characteristics present an escape or leakage risk [8]. There are two phenomena that make up this subject, sorption and diffusion; the subject of this paper is sorption [4]. Other work was performed related to diffusion, but diffusion is not the subject of this thesis. A list of references of similar work can be found in the reference section.

Sorption is characterized by the ability of a material to break or form bonds to the surface of another material. One could think of this as a phase change, and the Maxwellian distribution of energy or velocity of matter allows these interactions to occur, even at temperatures below points typically associated with full phase changes. Two primary mechanisms are found in sorption: physical and chemical, and they are the subject of section two [7, 9].

## 1.2. Objectives

The objective of this research is to obtain measurements of silver (Ag) on IG-110 graphite and validate the process through Sr measurements. The results of Sr will be comparable to previous experiments mentioned in the next section. To our knowledge, no experimental data for fission product sorption on IG-110 graphite exists in the literature. The method used to experimentally obtain the data is a Knudsen Effusion Mass Spectrometry (KEMS) [10]. Over the past 50 years this has become the industry standard for such experiments.

The objectives of this work are to:

- **validate KEMS method by measurement of strontium.**
- **provide supporting characterization of IG-110 graphite and associated bonded metals.**
- **provide methodology to handle mass loss between pseudo-equilibrium data point.**
- **measure enthalpy of vaporization for Ag and Sr on IG-110 graphite and**
- **thus define process involved in IG-110 graphite adsorption isotherms for Ag.**

Literature investigation developed a good understanding of experimental ranges for isotherm examination. Thus, the focused areas of concentration and ranges are provided in Table 2.

**Table 2.** Experimental table summary of objectives.

<b>Metal Material</b>	<b>Target Concentration Range [mmol/kg]</b>	<b>Target Temperature Range (K)</b>
Strontium (Sr)	1000 – 10	1100 - 1600
Silver (Ag)	1000 – 10	1100 - 1400

Note that some of the objectives are outside direct data acquisition. For reasons which will be discussed later, the concentration data during the KEMS experiment required interpolation. This information can be found in Chapter 4 Section 5 and Appendix 1d. This deviated slightly from previous techniques which involved radioactive material. However, the underlying experiment and instrumentation used are the same. This highlights the importance of validation with Sr. The method implemented is robust, based on theory and expands the feasibility of performing these experiments. The method is accompanied with a discussion on uncertainty and error, which assures the quality of data.

## CHAPTER 2. REVIEW OF PREVIOUS WORK

The key concepts needed to understand fission product sorption and development of methodologies center around adsorption physics. This section includes a brief review of current methods and work regarding adsorption and fission product sorption on graphite.

### **2.1. Adsorption**

Adsorption, within the context of this paper, is identified as the process of gas, atoms, or molecules accumulating on the surface of a solid. The solid and gas are called the adsorbent and adsorbate, respectively. This interaction is typically characterized by two primary drivers, the van der Waals force and chemical bonds [11, 12]. An adsorption process driven by van der Waals force is called physisorption (also called physical adsorption), whereas the one driven by chemical bonds is called chemisorption [4].

Physisorption occurs at particular pressures and temperatures and requires no activation energy, like condensation. The weak bonding associated with physisorption causes it to be reversible. Examples of this can be found in removing material by reducing pressure or increasing temperature, or adding material by reversing the aforementioned processes. In contrast, chemisorption depends on surface composition of the adsorbent and has characteristic activation energy corresponding to a chemical reaction [4, 7, 11]. Since it is characterized by a binding energy, the process is recognized as irreversible at a set of conditions, and only occurs to form a monolayer. Physisorption

contributes to the formation of many layers of adsorbed species, whereas chemisorption is the first layer of the sorbed species.

There are two primary experimental approaches to measure adsorption and the associated heat of reaction [13]. The first method is a static system, in which a fixed amount of adsorbate is introduced to the adsorbent or part of the adsorbent to start the process. Upon achieving equilibrium, both the gas and solid phase concentration of the adsorbate are measured. The second method is referred to as a dynamic or breakthrough system, wherein an inert gas carries an adsorbate over an adsorbent until the inlet and outlet concentrations of the adsorbate are the same [13]. The concentration profile, measured at the adsorption bed outlet is used to determine the equilibrium adsorbed amount as it corresponds to inlet concentration [4, 8].

**Table 3.** Summary of some experimental systems used to study adsorption. Note the method is referring to measurement of concentrations [4]

<b>1<sup>st</sup> Author</b>	<b>Year</b>	<b>Apparatus</b>	<b>Method</b>	<b>Data Type</b>
Connor [14]	1961	Static	Gravimetric	Isotherm
Salzano [15]	1961	Static	Radiotracer	Isobar
Salzano [16]	1964	Static	Radiotracer	Isobar
General Atomic [17, 18]	1967	Static	Radiotracer	Isotherm
Iwamoto [19]	1968	Static & Dynamic	Radiotracer	Isobar
Osborne [20]	1976	Static	Radiotracer	Isotherm
Lorenz [21]	1982	Dynamic	Radiotracer	Isotherm

Distinguishing between the two adsorption pathways can be unclear and thus experiments are repeated and a lot of data are required. Adsorption measurements are characterized by the amount of adsorbed material on the surface at equilibrium with the gas phase concentration at a specific temperature.

Mathematically, it is expressed as [9, 11, 13]:

$$c = f(P, T) \tag{1}$$

$c$  indicates the surface concentration and  $P$  is the partial pressure of the adsorbing species.  $T$  is the temperature of the system. Measurements are done by holding one of these constant and measuring the other two. The resulting data most commonly leads to a plot, called the adsorption isotherm. The graph is usually created along many temperatures and over a series of measurements whereby the full description of the adsorption behavior can be discovered.

## 2.2. Fission Product Isotherms

Fission product sorption on graphite isotherms relate fission product partial pressure to concentration in the sorbent carbon structure. The relevance of this measurement is to ascertain fission product release at the carbon boundaries for reactor safety models. Further, to calculate the transport of fission products at specific boundary conditions, one must have the enthalpy of vaporization and diffusion coefficients [17, 10].

For these measurements, historically one key apparatus has been used most frequently, the Knudsen Effusion Mass Spectrometer (KEMS) [10]. Primary experimenters in the field include General Atomic's Myers & Bell [18] and Hilpert et al. of the German Institute for Applied Physical Chemistry, Nuclear Research Center [22]. The method implemented used a radiotracer, which operates as a static measuring device with the aim to obtain isotherms. The Knudsen effusion cell acted as a containment device allowing for temperature control and allowing for localized equilibrium. The emission from the device can then be ionized and characterized by a mass spectrometer. This method was popularized by the experimental work of Myers and Bell [17, 18] and Hilpert et al. [22, 23, 24], studying strontium and cesium interaction with graphite. A more in-depth description will follow.

To understand their work, one must look at the continuation of theory from Equation 1. Much research has been dedicated to refining the fundamental understanding of sorption. One key facet is the energy required to cause the sorption process, in either a desorption or adsorption manner. This energy, the enthalpy of vaporization, is a key metric in phase changes, and is larger for chemisorption. Incorporating thermodynamic

relationships into Maxwell's relations can result in the following relation between pressure (p), temperature (T), and enthalpy ( $\Delta H$ ). R is the ideal gas constant [12, 25, 26].

$$\frac{dp}{p} = \frac{\Delta H'}{R} \frac{dT}{T^2} \quad (2)$$

where  $\Delta H'$  is the enthalpy per mole. Solving the above equation for pressure yields:

$$\ln(p) = \frac{\Delta H'}{RT} + A \quad (3)$$

Typically one creates a general plot relating to the inverse of temperature:

$$\ln(p) = A + \frac{B}{T} \quad (4)$$

Here B is roughly the enthalpy of vaporization over R, and A is a constant associated with the chemical system. Other models have been developed to more accurately account for deviations from ideality [27, 28]. Thermodynamic understanding of isotherms was expanded by the works of Freundlich, Henry and Langmuir. Starting with a base equation for an isotherm developed by Freundlich [6, 17, 29]:

$$\ln P_F = \left( A + \frac{B}{T} \right) + \left( D + \frac{E}{T} \right) \ln C_s \quad (5)$$

The constants A, B, D, and E are empirical and developed from fitting the data.  $C_s$  is surface concentration. It became apparent to Henry and Langmuir that at lower concentrations and pressures, the correlation needed some improvement. The primary improvement was determining a transition concentration,  $C_t$ , at which their regime would have a dominant form [6, 17, 29, 30]:

$$\ln P_H = \left( A + \frac{B}{T} \right) + \left( D - 1 + \frac{E}{T} \right) \ln C_t + \ln C_s \quad (6)$$

In some cases, the transition concentration is indeterminable; thus, one can define the transition concentration,  $C_t$ , as [6, 27, 29]:

$$\ln C_t = d_1 - d_2 T \quad (7)$$

Most theory of sorption, designates  $C_s$  as  $C_g$ . A key assumption, is that the gas concentration is directly above the surface of the material and is in equilibrium with the concentration at the surface. This assumption drives the need for confined measurements and significant control of the environment to acquire good data.

### 2.3. Technique and Previous Results

The Knudsen Effusion Mass Spectrometry (KEMS) technique [10] has been used for previous experimental acquisition of fission product sorption. It has the advantage of temperature, pressure and sample concentration control [23, 26].

KEMS experimentation is broadly responsible for our current understanding of fission product transport through its provision of a means to measure isotherm conditions, relating concentration to pressure [27]. For fission product sorption of metals on graphite, many other challenges relating to purity and oxidization occur, and only a limited number of data sets are available. The two primary sets of data that are available correspond to the work of Myers and Bell [17, 18] and Hilpert et al. [22, 23, 24] from the 1970s and '80s. Both groups used a combination of an isopiestic method and Knudsen Effusion Mass Spectrometry. We will describe the historical evolution of these methods.

Isopiestic is defined as “of, related to, or marked by equal pressure” [31]. Thus the isopiestic method indicates a constant pressure, which in this case, occurs in a system first set to a specific temperature and then allowed to reach static pressure [17, 18]. A measurement is taken and then a new temperature is selected. Myers and Bell [17, 18] measured concentration and pressure for two substrates in a system at a given temperature. A radioactive tracer of deposited metal on one of the substrates was isolated from the second substrate through a valved tube; the system was then brought to vacuum. The temperature was set and the system was allowed to reach uniform temperature. The valve was then opened and by constantly measuring the radioactivity of both substrates, equilibrium could be established when the two substrates had equal radioactivity. At this point, the pressure was measured before ending the experiment by evacuation, nitrogen

filling and cooling. The final surface concentration was then measured for each substrate [17, 18]. This created data for one point. Difficulties arose due to contamination by deposition onto the surface of experimental chambers and the large use of resources (time and substrates) to achieve one point. To alleviate these difficulties and improve upon the measurements, they switched to using a set of Knudsen cells as their isopiestic chambers. Additionally, they could dynamically measure the pressure through ionization and detection of the effusing species, which basically describes the task of a mass spectrometer. Through the isopiestic experiments, Myers and Bell found that tungsten and molybdenum were the least reactive containers, and thus they made their Knudsen cells with these materials. More detailed description, of the Knudsen Effusion Mass Spectroscopy is provided in the experimental section, as it is the method implemented for our experiments [17, 18, 28].

Myers and Bell focused on quantifying Cs and Sr diffusion and sorption in/on “fuel rod matrix material” and H-327 graphite. They obtained experimental data for Sr at temperatures ranging from 1300 to 1800 K and a concentration range of 10 to 0.01 mmol/kg on solid phase. Additionally, they studied the suppression effects of CO at pressures of  $3 \times 10^{-4}$  to  $5 \times 10^{-6}$  atm on the isotherm at temperatures between 1300 and 1500 K on H-327 using similar concentrations [27, 32]. They also tested irradiated graphite at constant Sr pressure of  $1.2 \times 10^{-6}$  atm. They found that increased irradiation and fluence resulted in higher surface concentrations at a given pressure. Their rationale was that smaller grain size and more defects allowed for higher sorption. They also obtained some data and used comparative methods of Sr on H-327 graphite to generate isotherms for the fuel rod matrix material. The matrix materials, which were carbon

based in nature, were Fort St. Vrain matrix, M-205, and calcined petroleum coke. Testing temperature ranged from 1250 K to 1800 K.

Myers and Bell's experiments with Cs were quite similar to [27] and [32]. In the Cs experiment they used KEMS and expanded the isopiestic experiment to incorporate multiple Knudsen cells also having the mass spectrometer available. They utilized this methodology to verify equilibrium measurements. The focus of the experiments was to create relatively reliable data around the 1273 K isotherm. They also added to the above list of materials mentioned for Sr by including P3JHAN graphite, H-451 graphite and Bar 675 Gilsocarbon graphite. They tested these other materials to verify some outliers at 1173 K. Additionally, they expanded the isotherm equations to contain confidence intervals. Further, this created complications for irradiation adjusted equations for the isotherms. Temperatures tested for these materials ranged from 1100 K to 1600 K and concentrations had a range of 10 to  $10^{-3}$  mmol/kg [27, 32].

One of the important highlights from their experiments was that the empirical parameters of isotherm transition from Henrian to Langmuir (Eqs. 5 and 6) could not be fully obtained isothermally (Eq. 7). Thus, transition concentration and associated uncertainties were a direct function of temperature. The transition concentration  $C_T$  appears to be much higher for the newer materials. Studies have been performed tabulating the empirical constants for  $A$ ,  $B$ ,  $D$ ,  $E$  and  $C_t$ . These similarly follow on tables 4 and 5 from two reviews. While it may not be initially clear, the units associated with each experiment cause variations in the reported values, as the fits are dependent on concentration, temperature, and pressure (CTP) points. Tables 4, 5, and 6 summarize these results in accordance with [18, 22, 27, 32].

**Table 4.** Sorption parameters for strontium in various graphite and materials. H-Henrian, F-Freundlich. Note the importance of studying the error associated with the isotherm. This is key to understanding the suitability of each model to experimental results

<b>Material</b>	<b>Units</b>	<b>A</b>	<b>B</b>	<b>D</b>	<b>E</b>	<b><math>C_T</math></b>
<b>A3-3 Matrix</b>	<i>Pa mol/(kg K)</i>	10.5	- 6222	- 1.591	6163	0.00015
<b>Fuel rod matrix</b>	<i>atm <math>\mu</math>mol/(g K)</i>	42.8	$2.85 \times 10^5$	- 8.52	$2.85 \times 10^4$	22.8
	$\sigma^2(\log p)] F = 5.16 - 5.812 \log C + 1.646(\log C)^2$ $\sigma^2(\log p)] H \cong 0.3$					
<b>H-327</b>	<i>atm <math>\mu</math>mol/(g K)</i>	9.44	$-4.24 \times 10^4$	- 0.57	$4.59 \times 10^3$	0.12
$\sigma^2(\log p)] F = 0.0239 - 0.0321 \log C + 0.0302(\log C)^2$ $\sigma^2(\log p)] H \cong 0.079$						

**Table 5.** Sorption parameters for cesium in various graphite and materials. H-Henrian, F-Freundlich

<b>Material</b>	<b>Units</b>	<b>A</b>	<b>B</b>	<b>D</b>	<b>E</b>	<b>C<sub>T</sub></b>
<b>A3-3 Matrix</b>	<i>Pa mol/(kg K)</i>	3.604	1400	-3.118	6707	0.00113
<b>Fuel rod matrix</b>	<i>Pa mmol/(kg K)</i>	19.3	- 47,290	1518	4338	*below
<b>1974-exp</b>		$\ln C_T = 3.397 - 6.15 \times 10^{-4} T$ $\sigma^2(\log p)] F = 0.42 ; ; \sigma^2(\log p)] H = 0.76$				
<b>Fuel rod matrix</b>	<i>atm <math>\mu</math>mol/(g K)</i>	8.39	38,300	- 0.5	4100	4
<b>1976-calc</b>		$\sigma^2(\log p)] F = 1.643 - 0.00264 \log C + 0.01519(\log C)^2$ $\sigma^2(\log p)] H = 0.114 - 0.050 \log C + 0.0212(\log C)^2$				
<b>H-451</b>	<i>Pa mmol/(kg K)</i>	24	- 35,730	- 1.561	6123	*below
		$\ln C_T = 2.035 - 1.786 \times 10^{-3} T$ $\sigma^2(\log p)] F = 0.79 ; ; \sigma^2(\log p)] H = 1.12$				
<b>H-327</b>	<i>Pa mmol/(kg K)</i>	19.747	- 30,368	-2.077	6710	*below
<b>1973-exp</b>		$\ln C_T = 0.545 - 7.775 \times 10^{-4} T$ $\sigma^2(\log p)] F = 0.424 ; ; \sigma^2(\log p)] H = 0.757$				
<b>H-327</b>	<i>Pa mmol/(kg K)</i>	7.09	27,600	- 0.5	4100	0.3
<b>1976-calc</b>		$\sigma^2(\log p)] F = 0.00134 - 0.00264 \log C + 0.01519(\log C)^2$ $\sigma^2(\log p)] H = 0.101 - 0.050 \log C + 0.0212(\log C)^2$				
<b>P<sub>3</sub>JHAN</b>	<i>Pa mmol/(kg K)</i>	27.73	- 42,153	- 4.1	8611	*below
		$\ln C_T = 2.386 - 1.86 \times 10^{-3} T$				

One of cumulative studies desired by Myers and Bell at General Atomics was irradiated versus unirradiated graphite; in particular, they studied cesium sorption on H-451 and

Table 6 has the results.

**Table 6.** Study of H-451 irradiated versus unirradiated of Cesium sorption. H-Henrian, F-Freundlich

Material	Units	A	B	D	E	$C_T$
H-451	$Pa\text{ mmol}/(kg\text{ K})$	24	- 35,730	- 1.561	6123	*below
<b>unirradiated</b>		$\ln C_T = 2.035 - 1.786 \times 10^{-3} T$ $\sigma^2(\log p)] F = 0.79 ; ; \sigma^2(\log p)] H = 1.12$				
H-451	$Pa\text{ mmol}/(kg\text{ K})$	42.64	- 47,290	1518	4338	*below
<b>irradiated</b>		$\ln C_T = 2.676 - 8.27 \times 10^{-4} T$ $\sigma^2(\log p)] F = 1.48 ; ; \sigma^2(\log p)] H = 1.48$				

Hilpert et al. experimented with Sr first and then Cs on A3-3 graphite, over the concentration range of 100 to  $10^{-3}$  mmol/kg. They covered a temperature range of 1000 to 1400 K for Cs and 950 to 2000 K for Sr [22, 24]. The Sr experiments did run to the  $10^{-4}$  concentration range. Most of the experimental data was obtained using the KEMS technique, but similar equilibrium data was obtained with the isopiestic method in the multi-Knudsen cell container set-up. Additionally, they used comparisons to obtain measurements of H-451 and coke resin binder through equilibrium data of the Sr experiments. Their full characterization of Sr adsorption through 1800 K was a significant contribution for H-451, as was their data for A3-3. The work of Hilpert et al. with Sr, as compared to the Cs experiments, posed difficulty in obtaining consistent data, due to the propensity of Sr to bond to resin. At very low concentrations, Hilpert et al. determined strong Sr-C bonds with enthalpies found experimentally to be in the range of 448 to 484 kJ/mol [22, 24].

Recently IG-110 and NBG-18 have been considered the new industry standards for graphite. Since experiments have proven to be expensive and quite time consuming, models have become more abundant.. Szlufarska at the University of Wisconsin completed a four-year modeling study on graphite. Utilizing density functional theory (DFT) calculations through the Vienna Ab initio Simulation Package (VASP) [32, 33], his goal was to define sorption of a fission product as having a binding energy on a graphite surface. The DOE's Nuclear Energy University Program (NEUP) final report has a more thorough explanation of how the program models sorption. A summary is provided in Figures 2 and 3 [27, 32].

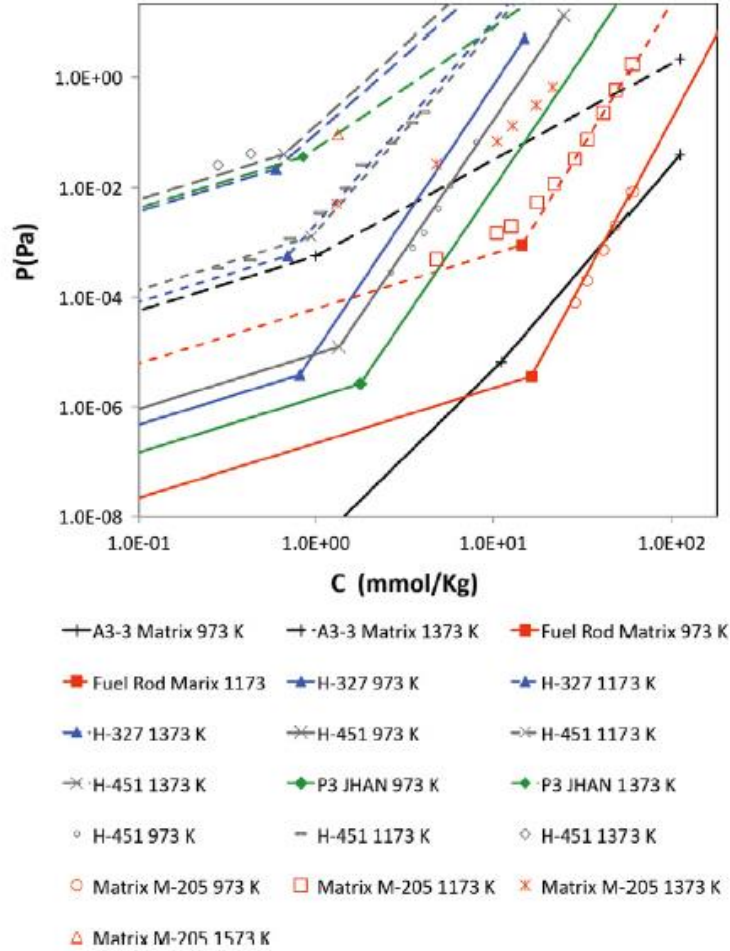


**Figure 2.** Cesium desorption from various graphite or fuel related materials. A3-3 and Fuel Rod Matrix experiments are from Hilpert et al. Myers et al. did experiments on H-327 graphite, H-451 graphite, P3 JHAN, and Matrix M-205 at various temperatures.

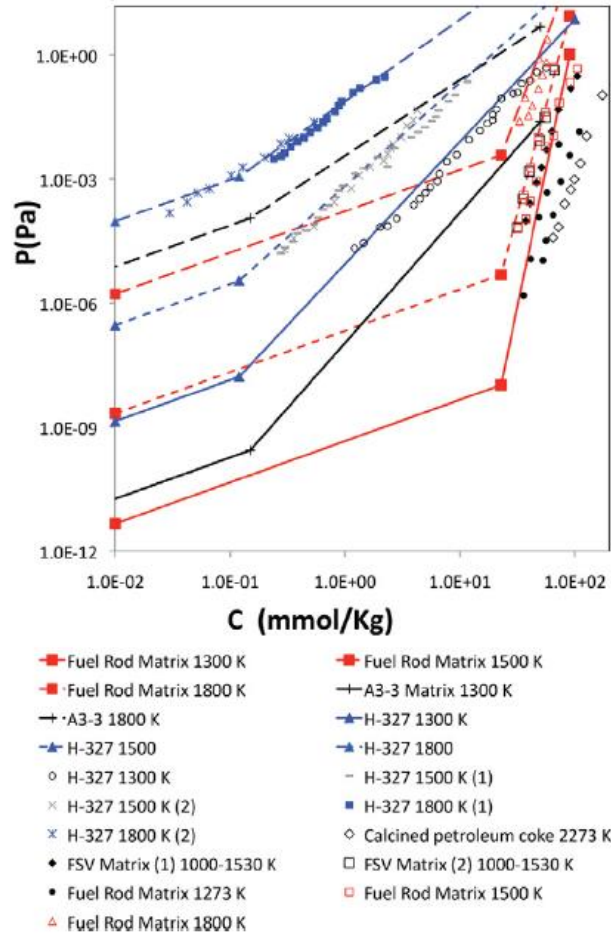


**Figure 3.** Strontium desorption from various graphite or fuel related materials. Again, the work of Hilper et al. make up the first two items of the Fuel Rod Matrix and A3-3; Myers and Bell performed the rest.

Generally, one first models the graphite structure as graphene sheets with binding energies between carbon molecules and between sheets. Then using  $sp^2$  and  $sp^3$  hybridization ranges in conjunction with experimental data, one creates the chemical potential energy of an FP atom (adatom) attaching to different binding sites on the surface. This surface chemistry was modeled thoroughly using Cs and Sr as a primary adatom. From this, a binding energy relationship could be created, for various well-

defined types of graphite. Then, using the expected combination of graphite cell formation for IG-110 and NBG-18, the project aimed at creating isotherm lines for Cs and Sr sorption [27, 33].

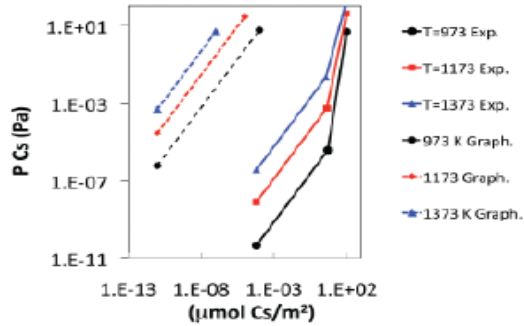


**Figure 4.** Cs sorption isotherms from experiments (Exp.) performed (averaging H-451, A3-3 and H-327) and DFT modeling (Graph).

Currently, as can be seen from the graphs above, modeling and expansion to include silver and create an understanding of IG-110 and NBG-18 will require experimentation. For this reason, the aim of this project is quite dramatic as it will couple sorption and diffusion characteristics for IG-110 and Ag. The results of the above experiments can be used to elucidate bonding configurations of Sr and Cs on carbon. Through use of the DFT computer programs such as VASP, and Package for Linear-combination of Atomic Orbitals (PLATO) further light has been shed on such bonding. Wang et al. also used their results to propose potential values for Ag bonding energy [27, 33, 34]. Full results of experimental and theoretically found binding energies, as well as enthalpies of vaporization, can be found in Appendix 3. To our knowledge there are no experimental data for Ag adsorption on graphite, and it is our purpose in this paper to obtain this data. The data can be used for reference in DFT simulations aimed at

understanding underlying mechanisms of metallic-carbon bonds and as reference material for source term computer programs.

## CHAPTER 3. INSTRUMENTATION AND MATERIAL PREPARATION

As noted earlier KEMS is the primary method of obtaining isotherm data for fission products bonded to graphite or similar structural material. Given the unique qualities of the instrument and our particular constraints, we discuss in good detail each aspect. An instrument breakdown is provided, as well as a sample preparation methodology, that was based on reviews of previous work.

### **3.1. Knudsen Effusion Mass Spectrometry**

#### 3.1.1. INTRODUCTION

This utilization of mass spectrometers was first implemented by Ionov to study vaporization of alkali metal halides in 1948. The Knudsen Effusion Cell (or Knudsen Cell) was developed by Martin Knudsen in the 1900s to confirm the kinetic theory of gases at near ideal round and cylindrical orifices [27]. A small sampling orifice allows for pseudo-equilibrium throughout the cell, which allows for sampling near ideal characteristics. Thus, the addition of the mass spectrometry allows for identification and quantification of the outlet of the Knudsen Cell [25].

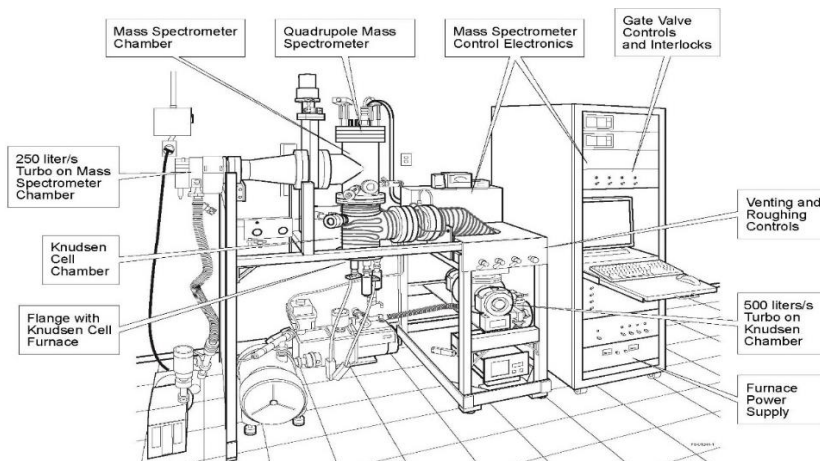


**Figure 5.** Knudsen Effusion mass spectrometer apparatus at Glenn research facility. This device demonstrates the importance of vacuum, isolation of effusing species, and temperature control. The instrument is coupled with a magnetic sector mass analyzer.

The figure above is certainly complex, but is typical of a Knudsen Effusion Mass Spectrometry set up. KEMS experimental apparatus consists of a mass spectrometer, ionization beam for the effusing species, vacuum support systems, heating support systems, and the Knudsen cell. Typically, the apparatus is primarily categorized by the cell alignment and adjustment infrastructure and the mass spectrometer [10, 26]. The system is described in greater detail in the following segment. The apparatus used for this experiment was a quadrupole mass spectrometer.

### 3.1.2. KNUDSEN CELL EFFUSION

The Knudsen cell is characterized by a small container with a small hole in the top surface and is assumed to reach equilibrium. The capsule is held in a vacuum space where the rate of molecules escaping through the hole is based on the rate at which molecules travel while scaling for the area of the hole to the containers surface area. The

pseudo-equilibrium assumption, between the gaseous and surface concentrations, holds if the mean free path of the vapor molecules is longer than the radius of the hole. The necessity of the vacuum presents itself, as air molecule interference would distort this path and cause contamination [30, 35].

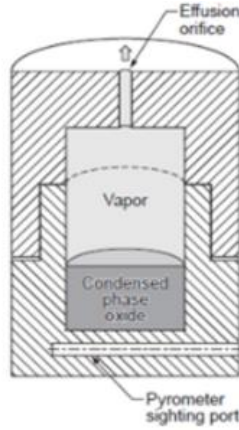


**Figure 6.** Sample image of a Knudsen cell. In the apparatus used, there is no sighting port for a pyrometer, as a thermocouple is used instead [25].

Following from the kinetic theory of gases Hertz and Knudsen obtained pressure,  $p_A^E$  with an expression relating flux,  $J_A$  (mol area<sup>-1</sup> s<sup>-1</sup>) of species A striking a surface of a closed container at equilibrium, E, [30, 35]:

$$J_A^E = \left(\frac{N_A}{\tilde{V}}\right) \left(\frac{\bar{s}_A}{4}\right) = \frac{p_A^E}{\sqrt{2\pi M_A R T}} \quad (8)$$

Here  $N_A$  is the Avogadro's number, and  $\tilde{V}$  is the specific volume of the sorbate species,  $\bar{s}_A$  is the average molecular speed,  $M_A$  is the molecular weight,  $T$  is absolute temperature, and  $R$  is the ideal gas constant. In the general case, not all molecules contacting a surface condense, but for an orifice, one is concerned with the molecules escaping.

The orifice of the Knudsen cell defines the maximum pressure and temperature at which the KEMS technique can be applied. In particular, the type of flow through the orifice needs to be a Knudsen flow, where molecule-molecule collision probability is low over the nominal dimensions of the orifice. The general criterion for effusion flow through an orifice is a Knudsen number,  $Kn$  greater than 8. This number is defined by the mean free path,  $\lambda$ , and the radius of the orifice is  $r_o$  [11, 30] thus

$$Kn = \frac{\lambda}{2r_o} \quad (9)$$

where the mean free path is defined as

$$\lambda = \frac{1}{\sqrt{2} \pi (P/RT) d^2} \quad (10)$$

This equation accounts for molecular properties such as molecular diameter,  $d$ , and cell parameters such as orifice radius,  $r_o$ .  $P$  in this case is total pressure,  $R, T$  are as defined earlier in [11] and [27]. Accounting for a real orifice requires a bit more analysis which can be explored in great detail in [11, 27]. Lumping characteristics of the orifice into two primary parameters are cross sectional area,  $A_o$  and the Clausing factor,  $W_c$ . The Clausing factor captures the shape of the orifice, possible irregularities along the orifice hole length, and the real boundary condition, which is at the edge of the hole hosting the vacuum. Finally, one can describe the molecular escape rate,  $\frac{dn_A}{dt}$ , of species ‘A’ through the orifice by adapting Eqs 7 and 8 [25, 36]:

$$\frac{dn_A}{dt} = \frac{A_o W_c p_A}{\sqrt{2\pi M_A R T}} \quad (11)$$

From the above equation, what one measures in a KEMS system requires ionizing the molecular beam, movement through the mass analyzer, and finally a counting by the

detector. To begin, one starts with the temperature, pressure, and alignment control to ensure flow is maintained in the Knudsen regime and properly enters the mass spectrometer [10].

### 3.1.3. AUXILIARY EQUIPMENT

The number of vacuum pumps in Figure 5 is typical of KEMS systems. They prevent overheating of the mass analyzer, depressurize the system, remove gaseous impurities before experimentation, and ensure effusing species does not build up to cause interference along the ionization path. Typical effusion pressures are in the millitorr to microtorr range; thus, only some of the sample is aligned along the beam path. Vacuum and heating times are the primary time limiting factor of each experiment [22, 25]. Each run requires heat ramping to be slow initially for any sorbed gas and surface moisture in the system. Additionally, cooling and depressuring before offloading and reloading samples require time.

Temperature verification and alignment are the primary reasons for including a camera or viewport. Temperature is measured through the viewport using a pyrometer, via measurement of thermally emitted optical spectrum electromagnetic waves [11]. As shown in Figure 5, we used a thermocouple supplanted use of a pyrometer. Our thermocouple was a Type B platinum-rhodium.

Only a small amount of the effusing species is properly aligned with the ionization beam to make it to the mass spectrometer. Thus, alignment control is essential. Alignment was accomplished through X-Y plane manipulators. This alignment would

occur during the calibration run and be checked at the initiation of each experimental run. Control can be coupled with software to handle multiple cells if necessary. While this would provide a more consistent and reliable measurement between cells, in our experiment a single cell flange was used. A drop is when the flange holding the Knudsen cell is isolated and removed to change samples or make internal adjustments. A drop thus requires time for the system to cool and pressure to be equalized, usually through a valve and cooling system. Another method of multiple cells in a rotational configuration is shown in Figure 7.

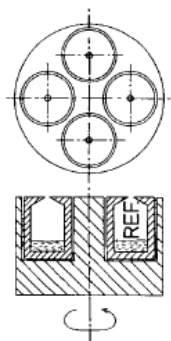


**Figure 7.** One of the sample configurations Hilpert, Gerads, and Kobertz [22] considered in performing their experiments. This rotational configuration ideally allows four cells to be aligned with the pyrometer and electron beam with one alignment step [27, 37]

The figure also denotes a “ref” cell, which indicates one of the four cells will be the reference cell. The reference cell is the primary alignment cell, and also contains the calibration material for the enthalpy of vaporization analysis.

Energy characterizes the mass spectrometry being performed. Below is a graphic demonstrating the different energies, characterized by temperature and pressure for each type of mass spectrometry [36].

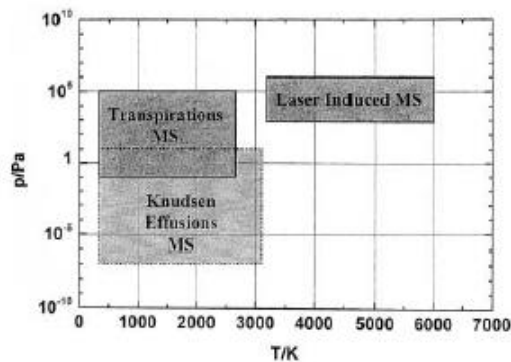


**Figure 8.** Graphic of the effusing species pressure and temperature characterizing the type of mass spectrometry.

The range of pressure and temperature of Knudsen effusion mass spectrometry (KEMS) allows some set-ups freedom from requiring a full ionization step. Transpiration MS, which utilizes an ionizing chemical species, can be used as a route; thus a Knudsen Cell may be used for operation. Ionizing chemicals result in a high pressure system, which is also possible with KEMS, but requires a secondary sealing mechanism for the chamber. Some setups utilize welded cells or a mechanical arm to combat the change of pressure from cell to spectrometer [36].

Laser induced MS results are very similar to KEMS, but the KEMS isolated chamber is not present, and the resulting temperature, causes a breakdown of desired components to be studied. In this sense, electron ionization (EI) is the most suitable for KEMS. In addition, this creates some selection measures as the beam can be increased or reduced in energy. This sampling method is critical when studying inorganics, as a beam of 70 eV breaks most bonds and creates elemental ionization. Finally, electron ionization yields the opportunity to redirect the effusing species causing a purer sampling technique.

The mass species path is never quite straight forward from effusion to mass analyzer, presenting the need for electron ionization, vacuum implementation, and close proximity.

#### 3.1.4. MASS ANALYZERS

In this experiment, there were two types of mass analyzers available at the National Aeronautics and Space Agency (NASA) Glenn Research facility. It is important to discuss each one and identify the differences between a time of flight (TOF) mass analyzer and a quadrupole (quad) mass analyzer. Mass analyzers are the devices that provide the equivalent capacity of ion filtration before they reach the detector. In a typical set up, one scans over the specified range and counts at each mass to charge ratio.

Magnetic sector mass analyzers were among the first configurations utilized in mass spectrometry [11, 23]. The nature of the analyzer yields high resolution and can be tuned to a specific range of mass selection. As the name implies, the magnetic sector mass analyzer utilizes a section of a magnet and voltage plates, with powers B and V, respectively. These powers are used to focus a beam with a specific charge, z. The result is a balancing of magnetic forces with the centripetal force of the arc of motion [11, 27].

$$F_B = ZvB == F_c = \frac{mv^2}{r} \quad (12)$$

Applying the kinetic energy of the beam in a to Eq. 6 gives the m/z equation:

$$\frac{m}{z} = \frac{B^2 r^2}{2V} \quad (13)$$

Thus, the relationship depends on the radius of curvature, r, magnetic field strength, B, and electric field strength, V. Since geometry and flight path play a significant role in studying the beam, the magnetic sector is typically considered in the broader

classification of the TOF analyzer [11, 36]. That being said, typical KEMS instruments utilize focusing components before the beam enters the mass analyzer paths and thus other TOF configurations become irrelevant compared to the magnetic sector. Further, these mass analyzers require significant maintenance and provide very nice mass to charge sensitivity. The aim of this experiment is concentration and sensitivity.

Quadrupole mass analyzers yield a nice balance of desired characteristics to output data.

Quadrupoles mass analyzers (QMAs) utilize opposing electrically charged rods to induce collisions and refine and focus the ion beam. The resulting electric field,  $\Phi_{(x,y)}$  creates two components,  $m/z$ , accounting for each direction perpendicular to the direction of motion based on electric field strength,  $\Phi_o$ . This results in velocities normal to the detector, but generates good resolution, further breaks down compounds, and requires a lower power than the magnetic sector. The frequency of alternating the electric field,  $\omega$ , plays a key role, as well [36, 38].

$$\Phi_{(x,y)} = \Phi_o \frac{(x^2 - y^2)}{r^2} = (x^2 - y^2) \frac{u - v \cos(\omega t)}{r^2} \quad (14)$$

$$u = q_u \frac{m}{z} \left( \frac{\omega^2 r_0^2}{8 e} \right) \quad (15)$$

$$v = q_u \frac{m}{z} \left( \frac{\omega^2 r_0^2}{4 e} \right) \quad (16)$$

To clarify,  $u$  is the velocity and  $q$  is the charge in the direction of charge motion. The beam begins to oscillate perpendicular to motion creating a cork-screw effect, which is described by the ‘ $v$ ’ velocity and rotational radius of ‘ $r$ ’. The high focusing power of the quadrupole mass analyzer results in a relatively narrow mass range, since mass outside this range will deflect into the poles and off the path of motion [36, 38].

The quadrupole mass analyzer (QMA) had well developed software associated with turning. Additionally, there are particular procedures to ensure consistence. The compactness of the QMA also adds to its appeal in the selection of a mass analyzer. Another consideration is power draw for operation, since so many components are involved, i.e., heating, alignment mechanics, electrical energy, pumping, etc. This power draw typically requires additional draws and specialized breakers. The variable field of the QMA does have a larger power requirement. In contrast the magnetic sector comes in two forms—an induced magnetic field, which requires much more power draw than QMA—and a stationary permanent magnet, which requires no power draw. The disadvantage of the permanent magnet is specialized shielding, introduction of specific components, and precautions needed when constructing around the magnet [36, 38].

Additionally, costs are reduced as detectors are typically included with the QMAs, since operation is performed via packaged software. Magnetic sectors, being more ‘hands-on’ design may reduce costs, as detector and analysis components are up to the builder. The size of a typical magnetic sector and TOF mass analyzers can also contribute to increased pumping down and heating times [11, 27, 36, 38].

Conclusively, the beam information is equally controlled via balancing electric with centripetal forces (magnetic sector/TOF), or opposing electric forces (QMA). The magnetic sector allows for broader peak generation since refining voltage and magnets can cause continuous scanning and refinement of data. This results in creating broad peaks over narrow  $m/z$  ranges, which is perfect for mass identification in a chemical process investigation. In this experiment, intensity identification is the desired piece of

accurate information, as  $m/z$  is known ahead of time [26, 28, 35]. This aspect signifies the preferable use of QMAs in sorption experiments using the KEMS technique.

## 3.2. Sample Preparation

### 3.2.1. GRAPHITE POWDER

Graphite powder was made from milling IG-110 blocks and sifting the powder between a 38  $\mu\text{m}$  and 20  $\mu\text{m}$  sieve, to yield roughly uniform grain size.



**Figure 9.** Shaker and sieves used to separate out the graphite powder.

The Brunauer-Emmett-Teller (BET) nitrogen-based experiment technique was used to determine porosity and tortuosity of the graphite powder.

**Table 7.** Results of nitrogen BET data yielding surface area and pore volume.

Initial Substrate Tests		
Graphite 38 $\mu\text{m}$	IG-110	NBG-18
Surface Area $\text{m}^2/\text{g}$	15.67	9.91
Pore volume $\text{cc/g}$	0.05075	0.0413

Our aim was to have our Sr data be comparable to previous experiments and then extend to Ag [8, 11]. Thus, we tested NBG-18 and IG-110 graphite initially, and then settled on IG-110 for further experimentation.

### 3.2.2. METAL NITRATE DECOMPOSITION

We followed the sample preparation methodology described previously and used by Hilpert et al [22, 24]. Metal nitrate concentrations of 1000 to 10  $\mu\text{g/ml}$  were pipetted onto samples of graphite powder. Samples were subsequently dried for 24 hours in a vacuum oven, and then transported to quartz tubes to be heat vacuumed sealed. A turbo pump was used to reduce pressure, and samples were heat sealed at 737 K and 0.1 Torr. The sealed tubes were then heated at 923 K (Ag) and 1173 K (Sr) for 72 hours to uniformly distribute the metal sample and complete the nitrate degradation. It was assumed that most of the nitrate had been removed in the initial sealing and oxidization was kept to a minimum. Analysis using EDS and SEM certainly verified this assumption for Ag, but showed some minor oxidization of Sr. We will explain this further in the sample characterization section.

### 3.2.3. INSTRUMENTAL NEUTRON ACTIVATION ANALYSIS

Instrumental neutron activation analysis (INAA) was used in a standard comparator experiment at the University of Missouri Research Reactor (MURR) facility. Standards were prepared gravimetrically from dried certified solutions of  $\text{AgNO}_3$  and  $\text{Sr}(\text{NO}_3)_2$ . The prepared powder was then irradiated with thermal flux of  $5.0 \times 10^{13}$  neutrons/( $\text{cm}^2 \text{ s}$ ) and the resulting gamma radiation was measured. Accurate amounts of metal present in the sample was determined by comparing with similar irradiation, decay and measurement times of standards [11].

**Table 8.** Table of nuclear reaction from neutron activation and key measurement information regarding gamma ray analysis for INAA

Radioactive Measurement			
Nuclide Reactions	Half Life	$\gamma$ - Energy	Irradiation Time
$^{107}\text{Ag} + \text{n} \rightarrow ^{108\text{m}}\text{Ag} \rightarrow ^{108}\text{Pd} + \gamma + \text{e}^+$	2.382 min	433.96 keV	5s
$^{86}\text{Sr} + \text{n} \rightarrow ^{87\text{m}}\text{Sr} \rightarrow ^{87}\text{Sr} + \gamma$	2.815 h	388.53 keV	20s

Two samples of the same powder were taken and tested. Concentrations are shown in Table 9. We, thus, verified that the samples had uniform concentration.

**Table 9.** Table of nuclear reaction from neutron activation, and key measurement information regarding gamma ray analysis for INAA

Powder Uniformity				
Sample Name	Powder Mass(mg)	Ag Mass ( $\mu\text{g}$ )	Concentration (mmol/kg)	Difference
Ag Powder A	3.65	90.78	230.56	<b>1.02%</b>
Ag Powder A.1	8.44	206.89	227.25	
Ag Powder B	2.26	15.99	65.61	<b>0.49%</b>
Ag Powder B.1	13.3	93.48	65.16	

Samples were prepared in the 1000 to 50 mmol/kg range. Specific concentrations are presented in the experimental matrix presented later. The samples were uniform within a milligram, and we investigated the samples further through high magnification imagery and X-ray spectroscopy.

#### 3.2.4. SCANNING ELECTRON MICROSCOPY AND ENERGY DISPERSIVE X-RAY SPECTROSCOPY

Image analysis and targeted spectroscopy were used to characterize bonding and metal dispersion or concentration in the pre/post-KEMS samples. For imaging, we used scanning electron microscopy (SEM). SEM coupled with energy dispersive X-ray spectroscopy (EDS) reveals visually the morphology, chemical composition, structure, and special variations in the sample [39, 40]. The instruments used were a Hitachi 4700 FE SEM at NASA Glenn Research Center and a Helios FIB and elemental mapping tool (Aztec by Oxford Instruments) at the Swagelok Center for surface analysis of materials (SCSAM) at the Case Western Reserve University.

Non-conductive samples are generally coated with a conductive material to avoid charging under the electron beam. In the case of our graphite substrate, conductive coating was not necessary for our short testing time frame [39]. Longer times could have potentially led to drift and heating. The process was taken as a destructive process, so images were taken in many locations, and of a small contingent of the sample.

Energy dispersive X-ray spectroscopy (EDS) uses the characteristic X-ray data to obtain relative quantities of atomic number over the scanning area, using a unitless spectroscopy signal received as counts [11, 39]. One typically calibrates this to standards or accepts the data as relative or qualitative. Given our unique samples, no standards were available for comparison, so the EDS data was taken as relative.

## CHAPTER 4. METHODS FOR CALIBRATION AND DATA ACQUISITION AND ANALYSIS

KEMS is a highly sensitive technique for measuring vapor pressures [17]. As such, the underlying concepts are extremely important to understand and review. How spectrometric analysis is performed and adjusted for various constraints, results in the need for multiple calibrations. Data points must be understood and related back to the multiple physical events the sample experiences in the chamber. For that to happen, the data is analyzed throughout the experiment and compared with the before and after studies of the samples. Finally using theory, we can interpolate our results to obtain better defined data points.

### 4.1. Spectrometry Analysis

The basic equation for mass spectrometry is typically presented as [11, 27, 28]

$$p = \frac{k I T}{\sigma} \quad (17)$$

where  $p$  is pressure,  $T$  is temperature,  $\sigma$  is captured cross section of the ion in the ionization step and  $I$  is intensity from the detector. Finally,  $k$  is the calibration constant for the apparatus as typically  $\sigma$  is the only piece considered fundamental to the system. Note this was kept general, although more clarity is certainly needed. To begin, one refers to the general premise, for a given species, A:

$$I_A \propto \dot{m}_A \quad (18)$$

From this assumption one generally attempts to relate  $\frac{dn_A}{dt}$ , or accounting for molecular to mass conversion,  $\dot{m}_A$  to  $I_A$ , and to be more precise, one must add the potential intensities of  $\frac{m}{z}$  measured by the detector.

A more formal equation 17 can then be written as [11, 27, 28]:

$$p_A = k \cdot T \cdot \frac{\sum_i I_{A,i}}{\sigma_A} \quad (19)$$

Typically, measurements are taken at a particular  $\frac{m}{z}$  ratio, and the potential of secondary effects are captured in a branching factor for a particular intensity,  $\gamma_i$ :

$$p_A = k \cdot T \cdot \frac{I_{A,i}}{\gamma_i \sigma_A} \quad (20)$$

In KEMS, three quantities can be measured quantities,  $T$ ,  $I_{A,i}$ , and  $p_A$ , two quantities are fundamental to the material  $\gamma_i$ ,  $\sigma_A$ , and one lumps the complicated effects and changes them into the calibration constant,  $k$  [11, 27, 28]. Focusing on physical aspects of the Knudsen Cell, the literature has defined  $k$  as [9, 11, 27, 28]:

$$k = \frac{\sigma_A}{\bar{I}_A T} \cdot \frac{1}{A_{OWC}} \cdot \sqrt{\frac{2\pi RT}{M_A}} \cdot \frac{dm_A}{dt} \quad (21)$$

$\frac{dm_A}{dt}$  is the mass loss rate similar to equation 11.  $\bar{I}_A$ , notation is used to describe the average property of intensity measured in a concise manner. Performing a mass loss experiment, one can validate some of these effects. Since the Clausius factor has much discussion on its formal representation, performing a calibration typically sticks to performing measurements based on the simplified Eq. 17 [9]. In this calibration one measures  $T$  and  $I_{A,i}$  and refers to documented values of  $p_A(T)$ . One couples this calibration experiment with a enthalpy of vaporization experiment to reduce the degrees of freedom. There are two key points in that calibration, the onset of melting temperature  $T_m$  and the resulting constant volume heat of vaporization,  $\Delta H_{vap}(A)$ .

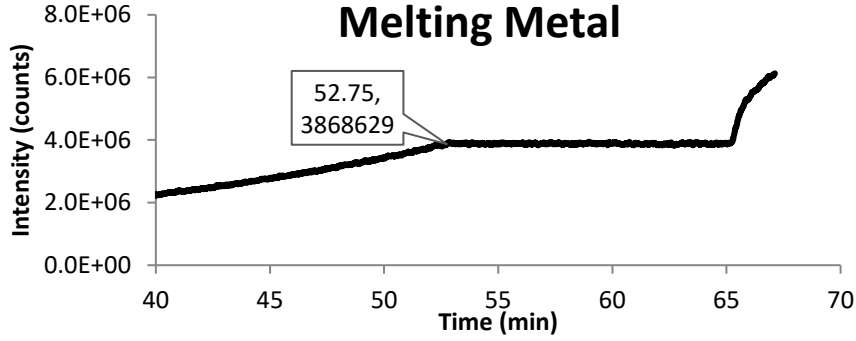


**Figure 10.** This figure was an experiment performed on 08-04-2015 and involved melting of silver in an alumina cell. The experiment data had a call out at the onset of melting, and demonstrated a good melting via flat intensity as temperature is ramped.

The melting data as presented above is coupled with temperature versus time, to determine the temperature onset of melting [11, 41]. Referring to the thermodynamics section, Eq.4 demonstrates that plot  $\frac{1}{T}$  versus  $\ln(p)$  or  $\ln\left(k \cdot \frac{I_{A,i}}{\gamma_i \sigma_A} \cdot T\right)$  as substitution will allow, should result in the heat of reaction; in particular, the reaction of gasification from a liquid, such as melting and condensing. Since one is looking for alignment in the melting experiment via temperature one anticipates a certain error in temperature [28]:

$$\Delta T_c = T_{m,obs} - T_{m,lit} \quad (22)$$

Observed and literature noted temperatures are abbreviated for temperature of melting. It is also important to note that once one adjusts for this temperature, they can determine their experimental error by observing

$$\%E \approx \frac{|\Delta H_{Obs} - \Delta H_{lit}|}{\Delta H_{lit}} \quad (23)$$

In particular, one aims for as little relative error as possible and attempts to get within 5% of literature values;  $\Delta H$  is a simplified format of implied volumetric and specie constraints.

As noted in the sample experiment, the two common metals used for this calibration experiment are silver, Ag, and gold, Au. To convert from one species to another, but keeping the same calibration constant, one just implements a ratio analysis:

$$p_A = k \cdot \frac{\sigma_{Ag}}{\sigma_A} \cdot \frac{\gamma_{Ag}}{\gamma_A} \cdot I_A \cdot T \quad (24)$$

This concludes the theoretical discussion of each piece of the KEMS apparatus [6, 24]. Now it is important to look at data previously gathered from similar experiments.

Figure 5 displays the use of multiple vacuum pump systems, a fully digital interface for the temperature control, and an analog system for gauges, valve controls and other startup/shutdown pieces. The primary difference between the work referenced by Myers and Bell [17, 18] and Hilpert et al. [22, 24] is the incompatibility to use radioactive materials. Thus, the use of radioactive tracers to determine instantaneous concentration is not a possibility. To compensate for this, the samples were prepared external to the system, rather than loaded in the KEMS. While this can allow for a reduction in preparation time, measurement time will increase.

Referencing the work done by Hilpert et al. [22, 24], graphite was loaded/soaked with metallic nitrate. for simplicity strontium (Sr) will be referenced as “the metal” from here. Our experiment included Sr and Ag. In the experiments of Hilbert et al., the sample was allowed to dry for 24 hours during the pump down of the system at 373 K. Then the sample in the KEMS system at vacuum was raised to 1323 K and held for six days to fully disassociate the nitrate, and drive off nitrogen oxide. The  $\text{Sr}(\text{NO}_3)_2$  had an initial concentration of radioactive isotope of Sr-85, and, thus, future concentration measurements could be determined by radioactivity [22].

Modifying for the use of a non-radioisotope system, our samples are prepared as powder and vacuum dried from the nitrate solution for more than 24 hours at ~393 K. This is followed by 100 mTorr vacuum seal at 773 K, a process that takes roughly 30 m to ensure no powder is lost. Then the samples, in vacuum sealed tubing are loaded for over 95 h at 1323 K. From here, the samples are cooled and a portion is removed for INAA analysis to determine concentration. The remainder of the sample undergoes a KEMS run, gathering intensity measurements at set pressures. The sample then returns to be ran in instrumental neutron activation analysis (INAA) to obtain a final concentration.

Now we can continue on the assumption that the linear mass loss rate is due to intensity relation in Eq. 17. We then integrate the entire amount of counts measured in time to obtain a relationship between the initial and final mass of strontium. Assuming no graphite powder is lost and a larger surface area is available, the mass initial and final results can be related in the following manner [6, 9, 11, 22, 27, 28]:

$$m_{t-initial} - m_{t-final} \sim \int_{t-initial}^{t-final} I(t) dt \quad (25)$$

From here at any count total, a mass/concentration in the sample can be found.

To complement this study, a mass loss experiment was performed, where a small amount of sample was removed at different time intervals to determine intermediate concentrations and verify the intensity analysis.

## 4.2. Equilibrium Points

The KEMS experiments have a significant impact on a sample at both chemical and physical levels. As noted in Eq. 17, the key elements for measurement are pressure and temperature.

In our instrument, specific ions with a known mass-to-charge ratio are continuously scanned, and the area under the peak is recorded in arbitrary units as intensity. The software then records ion intensity as a function of time, as shown in Figure 14. The peaks for Sr and Ag were both significantly above the background.

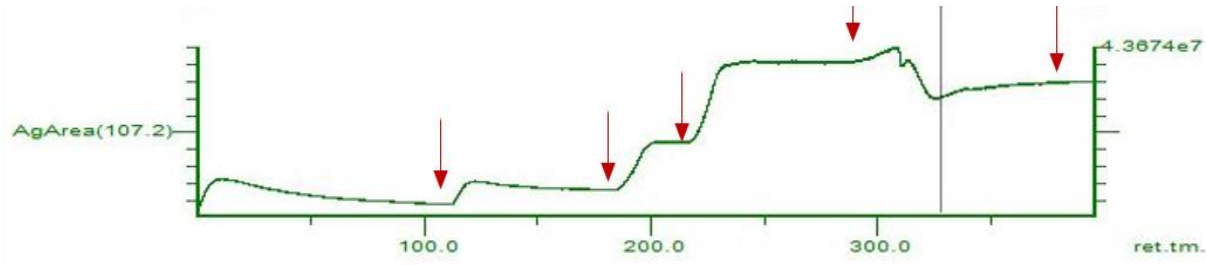


**Figure 11.** Visual raw output from Merlin™ software (Extel, Pittsburgh, PA) used at NASA-GRC. The Ag data is the area under the curve (AgArea 107.2); 107.2 is the m/z peak picked to perform the data study. The x-axis is time measured in minutes.

One must wait until equilibrium is reached to pick a point at a registered intensity for a given temperature. Equilibrium is indicated by a constant ion intensity with time. We set our scan times at 100 ms and averaged data over 5 scans. In contrast the temperature data was taken every minute. Thus, data was only taken at the equilibrium of intensity measured indicated by the red arrows in Figure 11. A typical data table is shown in Table 10.

**Table 10.** Data from calibration run number 2 using Ag melted in an alumina ceramic cell ( $\text{Al}_2\text{O}_3$ ). It is important to note that STD, is the standard deviation of the intensity as measured in counts. Thus, the % error, is the standard deviation of the intensity counts (divided by) the mean.

I (units)	% error	Time (min)	Start Time: 9:56 AM	Temp °C	Temp. K
$1.48 \times 10^6$	0.95%	12	10:08 AM	845.5	1119
$4.94 \times 10^6$	0.28%	39	10:35 AM	894.4	1168
$7.41 \times 10^6$	0.32%	75	11:11 AM	912.8	1186
$1.41 \times 10^7$	0.23%	125	12:01 PM	941.9	1215
$7.14 \times 10^6$	0.11%	170	12:46 PM	913.7	1187
$4.41 \times 10^6$	0.23%	196	1:12 PM	895.2	1169
$1.26 \times 10^7$	0.10%	255	2:11 PM	940.8	1214
$1.47 \times 10^6$	0.59%	292	2:48 PM	850.3	1123

Intensity as presented in units or counts, is an average number of a multitude of measured points. The standard deviation in the table is representative of the pseudo-equilibrium constraint over at least one minute's worth of streamed data. Statistics are available to ensure the point is an accurate description of equilibrium. Typically, a 2% threshold was required for all experiments. It is also important to note that the measured temperature, also has relative uncertainty due to thermocouple contact to cell, and calibrations are performed to identify specifically any error. The first calibration is a comparison of observed versus known temperature of Ag melting [11, 41]. The second calibration experiment obtains the instrument constant.

### 4.3. KEMS Calibrations

Pure Ag melted in an alumina cell was used as the calibration experiment since its thermodynamic properties are well documented, and it is an accepted International Temperature Scale (ITS)-90 standard. Specifically, its melting point is 1234 K, and the heat of vaporization is well-documented in the range of 1100 K to 1300 K [11, 41].

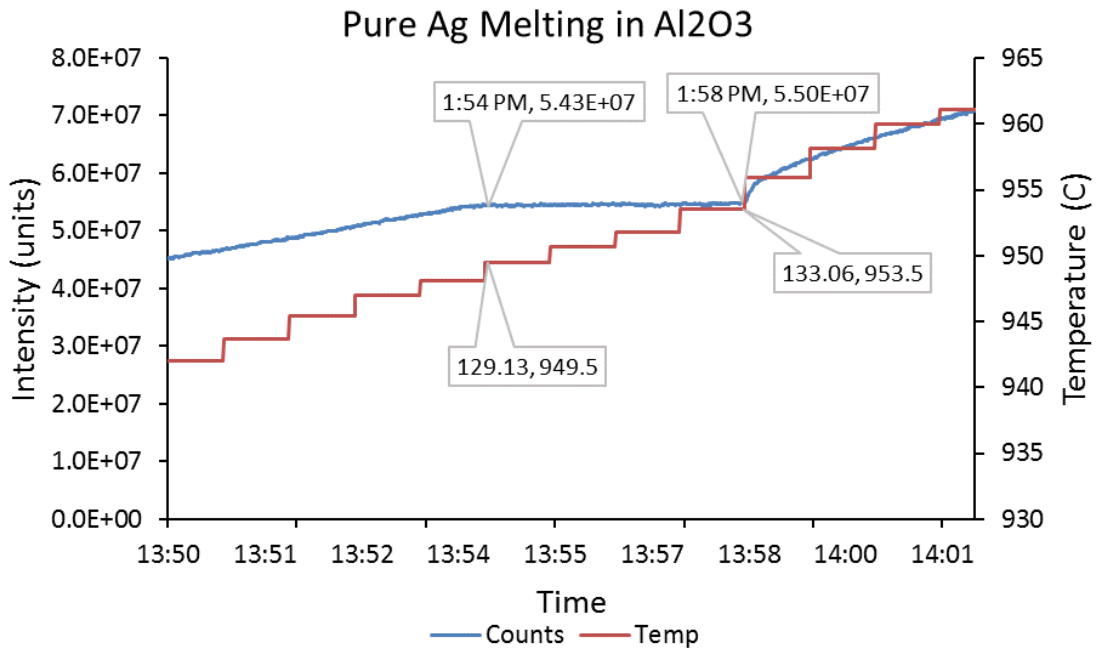


**Figure 12.** The above diagram shows the results of the melting phase of the calibration experiment.

Figure 12 is a commonly generated temperature ramp through the melting point. The plateau is the solid-liquid point as measured by a fixed expected vapor pressure during the melting transition. The onset of the plateau is taken as the temperature of melting for calibration purposes. The measured value here can be compared to the tabulated temperature of melting to obtain a temperature correction. The ion intensity at

the plateau is compared to the tabulated vapor pressure at melting and results in measurement of the calibration constant of Eq. 20 for the instrument.

A second method of temperature calibration is to measure a heat of vaporization, of Eq. 4, for a standard material and adjust the temperature correction until the heat of vaporization is close to the tabulated value. A series of points before melting can be observed and then to utilize the slope, one adjusts the temperature until the appropriate heat of vaporization for the tested temperature range is obtained. Figure 13 shows the implementation of this method [22, 25].

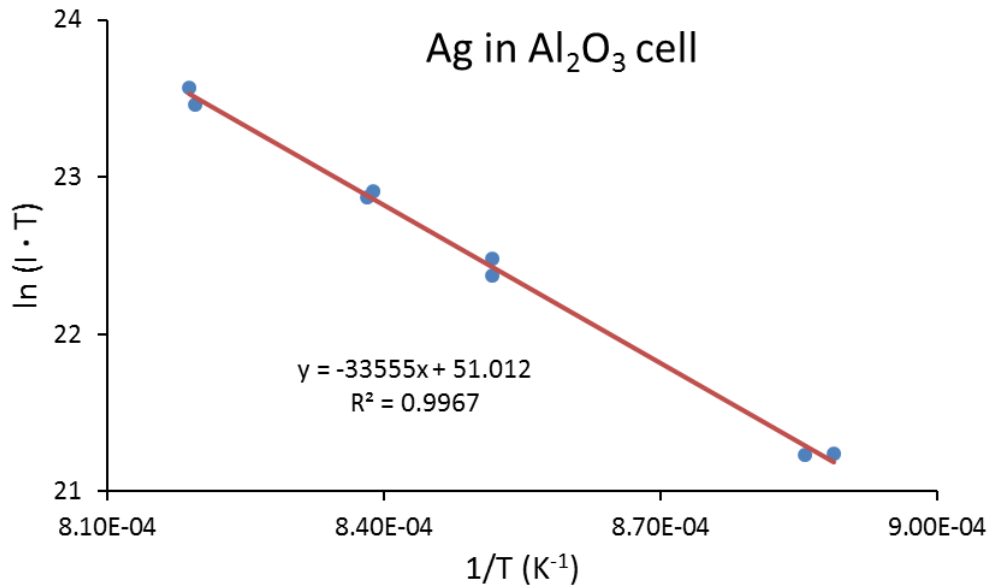


**Figure 13.** Data points are similar to Table 10.  $\Delta T$  is incorporated to fit the curve to  $\Delta H_{Ag,T}$  over this temperature range. Note I is intensity.

Ideally the temperature correction should be close for both methods. When it differed by several degrees, an average was taken. The large change was noted when some of the runs were discussed in the calibration section with the table of the runs.

#### 4.4. Preliminary Strontium Results

Specifically relating Eq. 24 to Ag and Sr was required for our preliminary results.

$$p_{Sr} = k \cdot \frac{\sigma_{Ag}}{\sigma_{Sr}} \cdot \frac{\gamma_{Ag}}{\gamma_{Sr}} \cdot I_{Sr} \cdot T \quad (26)$$

The net effect for these factors was multiplication of 0.33 for  $\frac{\sigma_{Ag}}{\sigma_{Sr}}$  and 0.91 for  $\frac{\gamma_{Ag}}{\gamma_{Sr}}$  on the calculation of the strontium pressure [22]. We performed some initial experiments on strontium, labeled as sample 10. There was noticeable drift in the intensity over time despite constant temperature. We attributed this to phase change or a continuous, effective concentration change in the sample.

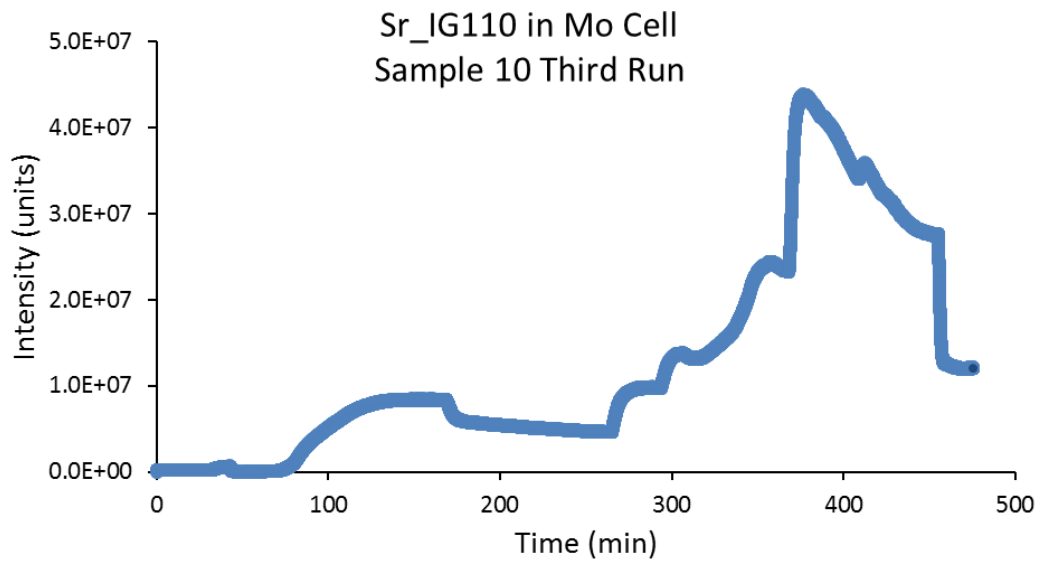


**Figure 14.** The third run of sample 10 shows that drift is still present. It is important to note that Sr 10 was run three times to check and address this issue.

Also note that all experiments can be characterized by enthalpy of vaporization as described in Eq. 4. In a pure material, this is noted as energy to break metal-metal bonds, but in our instance, it is the bonding energy of breaking the sorbed metal, M, to the

substrate, IG-110. Note that enthalpy of sorption and vaporization are synonymous effectively as the metal travels from the surface as a solid to gas. This is a consequence of the assumption laid out in the theory section, stating that the concentration in the gas phase right above the sample (which is not considered part of the gaseous area) is the same as the surface concentration,  $\Delta H_{M,IG110}$ , although, we refer to it generically as the enthalpy of vaporization. Similar to the calibration in Figure 13, we can represent these points in graphical form.

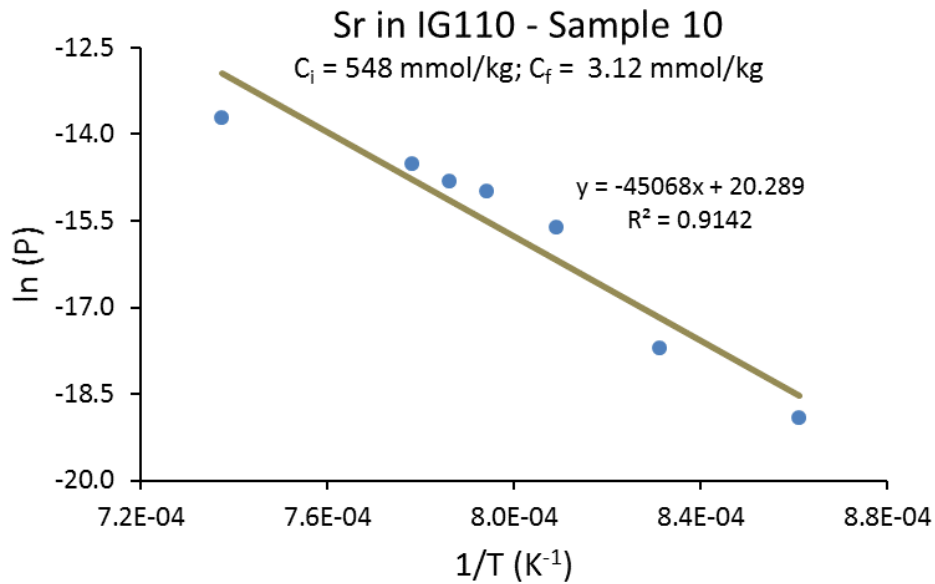


**Figure 15.** Collection of data points for Sr 10 run 3. It is important to note that the R<sup>2</sup> value creates a significantly uncertain value. The  $\Delta H_{Sr,IG110}$  comes to 375 kJ/mol in the temperature range of 1150 to 1350 K.

The above data, demonstrated an enthalpy of vaporization of 375 kJ/mol, which was comparable to the work of Hilpert et al. [22] at a concentration of 3.31 mmol/kg as shown in Table 12. Given the initial and final concentrations of sample 10, it is apparent that a significant portion of the strontium burned off. Additionally, Figure 15

demonstrates some parallel lines of the data. This led to the low statistical,  $R^2$  value. We attempted to alleviate this by proceeding with a “burn off” step to ensure stability at lower temperatures.

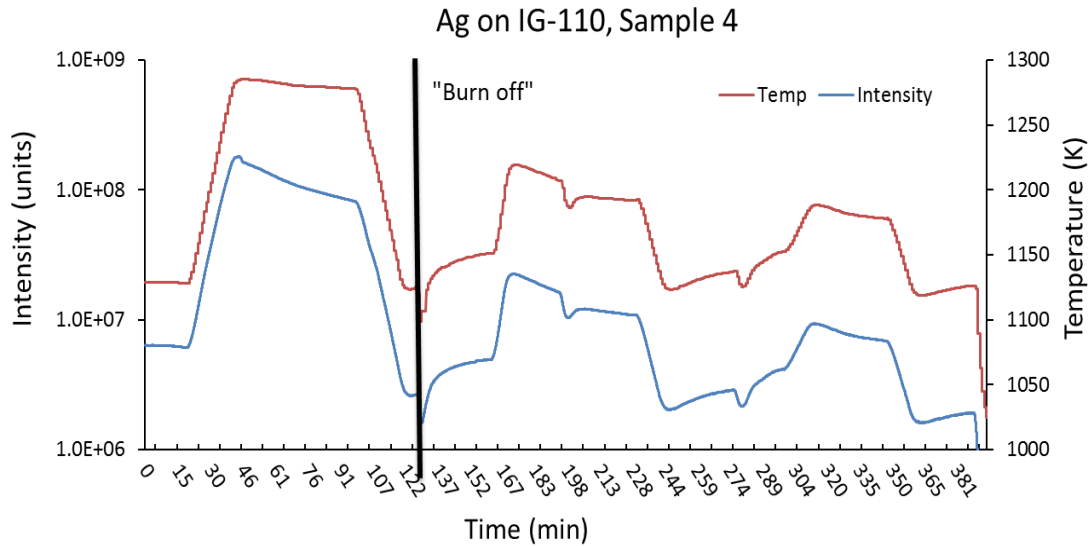


**Figure 16.** The figure is a log scale plot of the intensity counts of Ag sample 4. This sample can be characterized by its initial and final concentrations of 1062 and 426 mmol/kg. As noted before points should achieve equilibrium, we note instability in these attempted points before “burn off”.

Previous studies by Myers and Bell and by Hilpert et al. used radioactive tracers [17, 22], which allowed concentrations to be measured continuously. Our data required adjustments to be equally comparable in scope. The burn off was one such method. Unfortunately, some of the Ag samples (1,3) were ran too long during this phase and no data was obtained. While this was not ideal, it did lead to the establishment of a new approach to obtaining concentration data.

#### 4.5. Solid Phase Mass Estimation

Despite the burn off phase we attempted to verify that the theoretical mass loss rate is negligible through analysis of Eqs.11 and 24 for given temperatures and specified calibration constants. Using a mean value of calibration constants in the results section, Tables 11 and 12 show loss rates for mass and mole quantities. Note the mass loss rates

for Ag in Eq. 10. These mass loss rates can be modified by  $\sqrt{\frac{M_{Sr}}{M_{Ag}}}$  for Sr.

**Table 11.** Loss of silver calculated through Eq. 10 in micrograms per hour.

P (atm), T(K)	Mass Loss Rate ( $\mu\text{g/hr}$ )				
	1000	1100	1200	1300	1400
$1 \times 10^{-6}$	242.34	231.06	221.23	212.55	204.81
$1 \times 10^{-7}$	24.23	23.11	22.12	21.25	20.48
$1 \times 10^{-8}$	2.42	2.31	2.21	2.13	2.05
$1 \times 10^{-9}$	0.24	0.23	0.22	0.21	0.20

**Table 12.** Loss of silver calculated through Eq. 10 in nano-moles per hour.

P (atm), T(K)	Molar loss Rate (nmol/hr)				
	1000	1100	1200	1300	1400
$1 \times 10^{-6}$	2260.64	2155.43	2063.67	1982.71	1910.59
$1 \times 10^{-7}$	226.06	215.54	206.37	198.27	191.06
$1 \times 10^{-8}$	22.61	21.55	20.64	19.83	19.11
$1 \times 10^{-9}$	2.26	2.16	2.06	1.98	1.91

We note that measured equilibrium points require 30 minutes to achieve stability. From the tables above, we recognize that such time scales, temperatures and pressures will result in significant mass losses. We have measured initial and final concentrations, and given the mass of initial sample powder loaded, we can determine the change in mass of Ag and Sr burned off. We have given some details in Appendix 1c, but thorough analysis will follow.

**Table 13.** Strontium mass measurements before and after the experiment

Strontium Samples	Concentration (mmol/kg)		Sample Mass (mg)	Mass of Sr ( $\mu\text{g}$ )	
	Before	After		Before	After
<b>9</b>	32.62	2.65	83.21	237.9	19.3
<b>10</b>	547.94	3.12	192.82	9257.4	50.2
<b>11</b>	31.35	4.71	88.63	243.5	36.5
<b>13</b>	716.73	4.41	85.21	5351.2	30.9

**Table 14.** Silver Ag measurements before and after the experiment

Silver Sample	Concentration (mmol/kg)		Sample Mass (mg)	Mass of Ag ( $\mu\text{g}$ )	
	Before	After		Before	After
<b>1</b>	228.9	$4.275 \times 10^{-3}$	141.1	3484	$6.347 \times 10^{-2}$
<b>2</b>	395.3	5.161	107.8	4597	57.49
<b>3</b>	112.3	0.2489	83.39	1010	2.212
<b>4</b>	1062.0	426.2	74.97	8588	3199
<b>5</b>	65.4	1.769	90.28	636.7	17.11
<b>6</b>	376.4	16.4	104.3	4236	177.8
<b>7</b>	1266.6	743.4	115.2	15745	8674
<b>8</b>	27.7	2.604	134.2	401.2	37.60

Based on the above results it becomes necessary to identify concentrations at each equilibrium point. Using Eq. 21, we obtain  $\dot{m}(t)$  as a function of measured quantities,  $I$  and  $T$  [26, 27].

$$\dot{m}(t) = A_0 W_c \sqrt{\frac{M}{2\pi RT(t)}} \frac{k I(t) T(t)}{\sigma} \quad (27)$$

For a given concentration run we can combine the constants.

$$\dot{m}(t) = \frac{A_0 W_c k}{\sigma} \sqrt{\frac{M}{2\pi R}} * I(t) T(t)^{\frac{1}{2}} = \beta I(t) \sqrt{T(t)} \quad (28)$$

Further we recognize that we are attempting to reconcile the measured data at a given equilibrium time,  $\tau$ . At the fixed temperature we measure an integral quantity of  $I(t)$  as

$$I_{meas}(\tau) = \int_{\tau}^{\tau+\Delta t} I(t) dt = \overline{I(\tau)} \Delta t \quad (29)$$

We measure intensity in regular intervals; thus, we can approximate mass loss rate by

$$\dot{m}(\tau) = \beta \cdot \overline{I(\tau)} \cdot T(\tau)^{\frac{1}{2}} \cdot \Delta t = \beta \cdot I_{meas} \cdot \sqrt{T(\tau)} \quad (30)$$

From INAA, we have an initial and final measured mass of metal, which calculates to concentration, and then is converted into initial and final masses given the weights of powder loaded. Loss of mass affects the concentration through the denominator as well via the effective change in total mass. This is thoroughly shown in Appendix 1d and Tables 11 and 13. However, the total mass change is calculated as

$$m_i - m_f = \sum_{t=exp} \dot{m}(\tau) = \sum_{t=exp} \beta \cdot I_{meas}(\tau) \cdot \sqrt{T(t)} \quad (31)$$

or the change in mass at any given point in time  $\theta$ , can be found by the ratio of sums

$$\frac{m_i - m_\theta}{m_i - m_f} = \frac{\sum_{t=\theta} \beta \cdot I_{meas}(\tau) \cdot \sqrt{T(t)}}{\sum_{t=exp} \beta \cdot I_{meas} \cdot \sqrt{T(t)}} = \frac{\sum_{t=\theta} I_{meas}(\tau) \cdot \sqrt{T(t)}}{\sum_{t=exp} I_{meas} \cdot \sqrt{T(t)}} \quad (32)$$

The above solution yielded the interpolation of masses and concentrations along the measurement process [11]. Rather than trusting in some initial or final concentration or mass, we were able to interpolate our data. We used the final mass concentration and added back the mass loss indicated by above measurements. This added mass yielded the surface concentration as shown by the calculations in Appendix 1d. Matching between the initial and final concentrations, through burn off, both were aligned through the scaling factor of  $\beta$ . The final results in the next section demonstrate the reliability of this method, as they are in agreement with historical data for Sr. Furthermore, good statistics are associated with concentration data developed for Ag.

## CHAPTER 5. RESULTS

As noted earlier, results begin and end with the samples initial and final conditions. In this section, we review the results of characterization to achieve a better understanding of the data points obtained via KEMS. We perform this visually through SEM and EDS, as well as quantitatively using our KEMS data and pre- and post-INAA. Theory then provides the means to obtain higher level quantities of the adsorption phenomena, such as the enthalpy of vaporization, and the starting points of the isotherms for Ag. Additionally, we validate our technique through a comparison of the Sr results.

### 5.1. Sample Characterization

#### 5.1.1. CONCENTRATIONS

The experimental goal is to measure vapor pressure of a metal at various surface concentrations, and temperatures. It becomes a key component in compiling the data first as an enthalpy of vaporization and then as the distinguishing characteristic of the isotherm. Historical data for Sr spans temperatures of 1100–1900 K. In our experiments, our calibrations were performed using melting Ag, and to ensure accuracy we used temperatures between 1100–1500 K. This temperature range was selected since we aimed at using Sr experiments to validate the technique. Additionally, we anticipated Ag-C isotherm characteristics to be near Ag's melting temperature, as historical data determined no remaining Ag on graphite at higher temperatures. Ag melting temperature is 1234 K; thus, we selected a temperature range for Ag on graphite of 1000–1300K.

We used INAA to measure concentrations of metals (Sr and Ag) on graphite before and after KEMS experimentation and deduced concentrations on graphite during the KEMS measurements through a computation of evaporation losses as discussed in the previous section (from the vapor pressure measurements).

**Table 15.** Concentrations of Sr and Ag samples created for Knudsen effusion mass spectroscopy. Concentrations are given in millimole of sorbed metal per kg of sample or graphite powder metal mixture, typical of previous experiments.

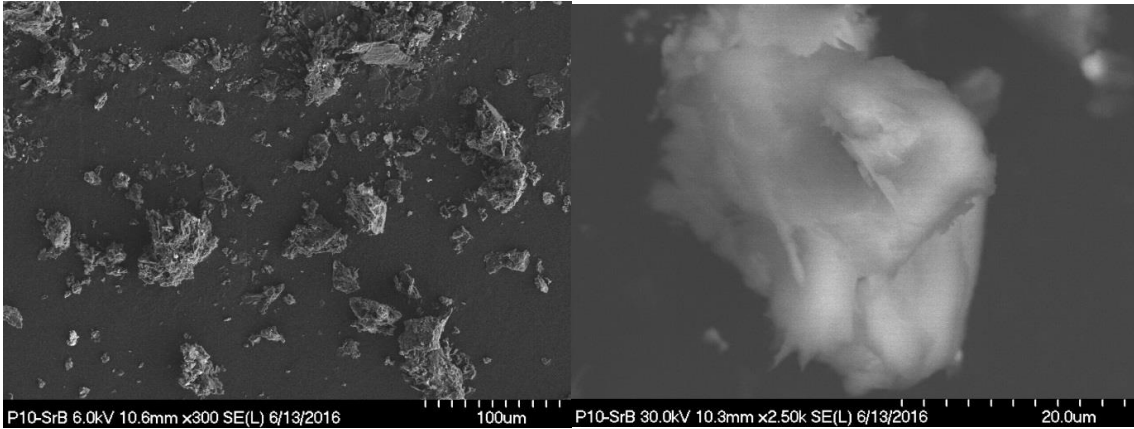
Sample Preparation Summary					
Sorbed Metal	Sample ID	Concentration Before		Concentration After	
		mmol/kg	g/g	mmol/kg	g/g
Sr	9	32.6	$2.86 \times 10^{-3}$	2.65	$2.32 \times 10^{-4}$
	10	547.9	$4.80 \times 10^{-2}$	3.12	$2.74 \times 10^{-4}$
	11	31.4	$2.75 \times 10^{-3}$	4.71	$4.12 \times 10^{-4}$
	13	717	$6.28 \times 10^{-2}$	4.41	$3.86 \times 10^{-4}$
Ag	1	229	$2.47 \times 10^{-2}$	$4.28 \times 10^{-3}$	$4.61 \times 10^{-7}$
	2	395	$4.26 \times 10^{-2}$	5.16	$5.54 \times 10^{-4}$
	3	112	$1.21 \times 10^{-2}$	0.249	$2.68 \times 10^{-5}$
	4	1062	$1.15 \times 10^{-1}$	426	$4.60 \times 10^{-2}$
	5	65.6	$7.08 \times 10^{-3}$	1.76	$1.90 \times 10^{-4}$
	6	377	$4.06 \times 10^{-2}$	16.4	$1.77 \times 10^{-3}$
	7	1267	$1.37 \times 10^{-1}$	743	$8.02 \times 10^{-2}$
	8	227	$2.45 \times 10^{-2}$	2.60	$2.81 \times 10^{-4}$

Concentrations are presented in Table 15, with two different concentration units for clarity. In the material science community weight percent is most common and to compare our prepared materials with those reported in literature [17] [22], molar concentration was also used. Samples prepared by Hilpert et al. ranged from 140 and 120 mmol/kg, Sr on A3-3. While they could perform the experiment continuously using the radioactive tracer method, their recorded concentrations for isotherm reaction did not begin until 88.5 mmol/kg and stopped at around 0.1 mmol/kg; thus, as prepared, our samples are comparable to those used in previous work.

### 5.1.2. QUALITATIVE IMAGING

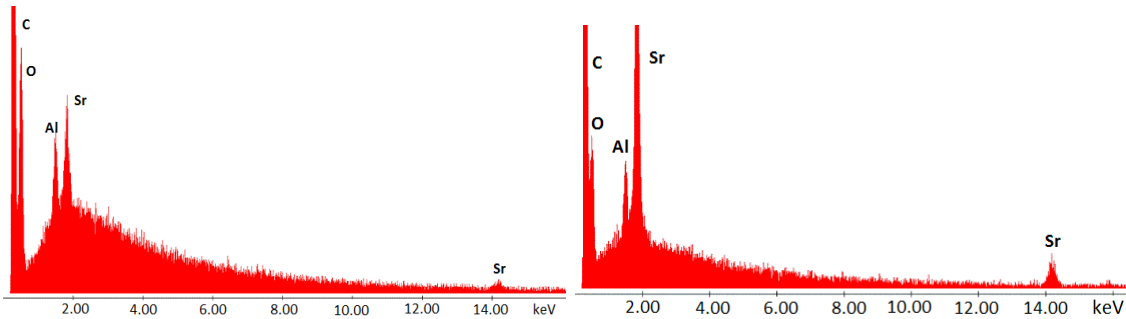
In addition to concentration, the bonding characteristics observable before and after the KEMS experiment provided insights. The bonding effects directly impact the sorption characteristics and underlying chemistry associated with the isotherm. Previous work led to anticipation of oxygen contamination during Sr impregnation of graphite. Fourier transform infrared spectroscopy (FTIR) was performed and yielded the presence of oxidation but could not distinguish between a Sr-O bond and a C-O bond in the presence of metal. Thus, we used microscopy, which also yielded insight into structure [42] [43].

Figures 17 and 18 present images of Sr dispersed on IG-110. Figure 18 is an enlarged portion of the central Sr particle in Figure 17. Images verified that most samples had carbon structures in the 38  $\mu\text{m}$  to 20  $\mu\text{m}$  range; although there is significant dispersion from this range, likely as a side-effect of processes performed in sample preparation.



**Figures 17 (left), 18 (right).** Left shows large dispersion of IG-110 with strontium present in sample number 10, as noted in Table 7. Right shows an enlarged portion of the center particle to illustrate the general size.

SEM coupled with EDS yielded information on the morphology, topography, and relative composition of the sample and allowed characterization of the metal on graphite samples (Figures 19 and 20) [30] [40] [44].



**Figures 19 (left), 20 (right).** The graph on the left shows the sample of strontium imaged before, but with targeting of the dark areas of the sample. Note that significant oxygen is present relative to strontium. Additionally, given the beam energy necessary to verify strontium's presence, as the X-axis is keV, there was significant scattering off the aluminum holder. The graph on the right shows the data taken at a brighter spot in the sample, particularly a zoomed in feature associated with Figure 18. This demonstrates strong strontium presence with less, but still present oxidation.

Images were taken for some of the Ag samples, to determine morphology and if similar oxidation was present. It is important to notice that for strontium, the oxygen concentrations ranged from 5 to 14% atomic relative to the carbon, strontium, and aluminum present. Note that aluminum is only present due to energy deposition depth reaching the back-plate aluminum material. It is quite possible to assume a significant portion of this oxygen could be due to surface adsorbed water, as graphite is very hydrophilic. Thus, after KEMS and a temporary heating experiment, EDS was performed, and it was determined that roughly 80% or more of the oxygen measured previously had been removed as shown in Figure 21.

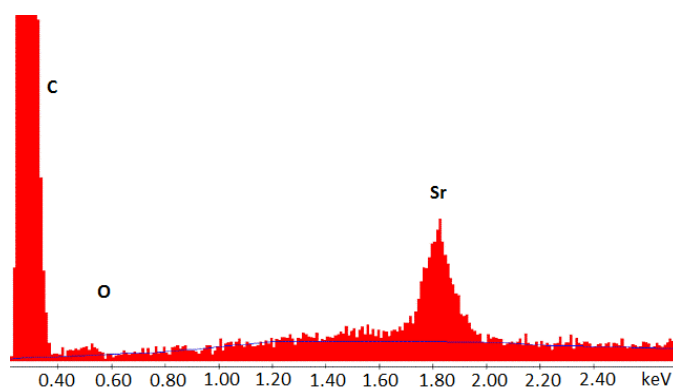
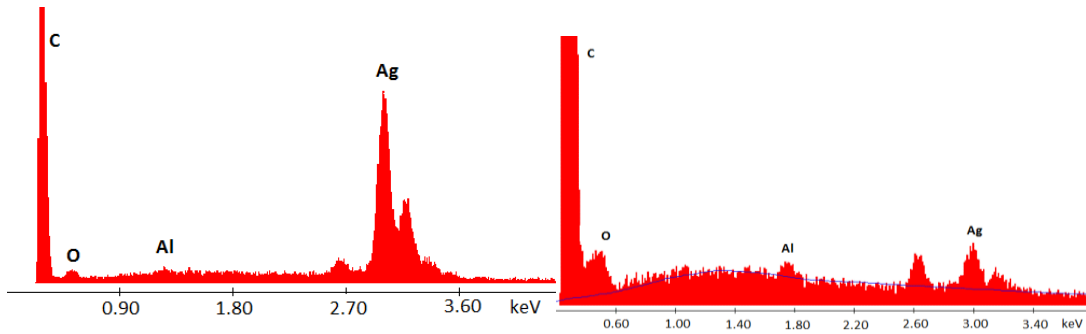


**Figure 21.** Post heating sample run for strontium 10. Heating was performed at roughly 737 K for 10 hours under vacuum. Additionally, the sample was then tested within an hour of being removed from the vacuum. This was taken at a bright spot and shows only 0.95% atomic oxygen versus 5% for Sr.

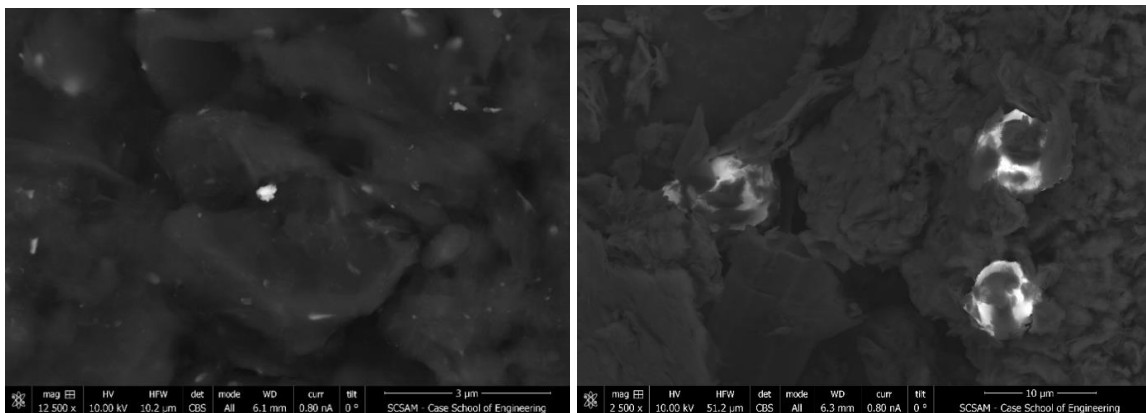
When compared to Ag, significant oxygen is present in the Sr samples. An example Ag plot was taken using sample number 4 at a bright spot. It demonstrated 15% Ag presence relative to negligible oxygen in Figure 22. Note that sorbed water was also present in Figure 23, as shown by an oxygen amount comparable to Ag. This is similar to preheated Sr in Figure 19.



**Figures 22 (left) and 23 (right).** This shows sample 4 of Ag before experiments were performed. The left graph shows one of the bright spots where Ag was present in high quantities of roughly 15% relative atomic. The right graph shows a dark spot with some Ag present but with comparable oxygen.

It was important to note that given the clear sorbed water, before running any experiment, samples were kept in a desiccator. Additionally, temperature ramping upward was slow to remove moisture and avoid over pressuring.

Back-scattered electron (BSE) imaging in the SEM was also quite useful for these samples [30, 40, 44]. In this mode, the heavier metals appear brighter, as shown in Figures 24 and 25.



**Figures 24 (left) and 25 (right).** These photos represent sample 6 of Ag on IG-110 graphite taken using back scattering electron filter. The photo on the left shows

significant distribution of Ag throughout graphite grains. The photo on the right shows embedded Ag after it has coagulated and formed clusters of high concentration.

Figure 24 of Ag on IG-110 demonstrates that sample preparation was successful in developing distributed metal uniformly throughout the graphite powder. By contrast, Figure 25 was taken after a KEMS experiment. The observed phenomena shows that Ag will preferentially sorb to itself and form these faceted super clusters between the graphite layers. Higher resolution of this faceting is imaged in Figure 26, where the Ag is identifiable by smoothness of the structure. Graphite bonds in graphene sheets typically occur in a non-uniform manner, yielding a sharp and layered look [29] [45].

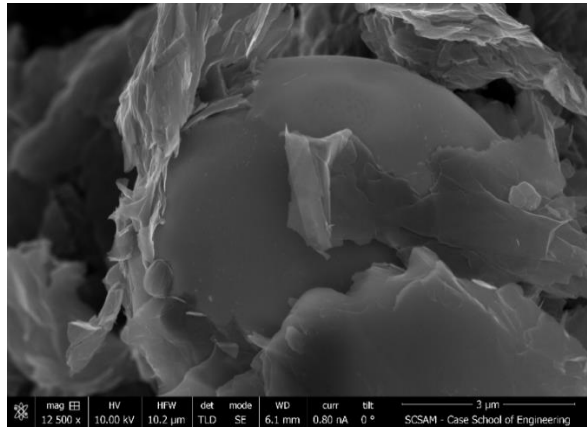


**Figure 26.** Ag (sample 6) in IG-110 post analysis, using secondary electron imaging.

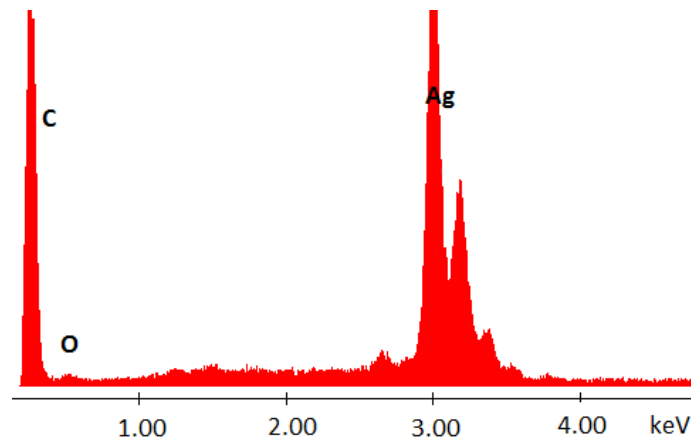


**Figure 27.** EDS of Ag (sample 6) in IG-110 post analysis based on Figure 11.

The reduction of oxygen post analysis relative to Figure 8 is striking and supports that sorbed water was all that remained (Figure 13). Additionally, the Ag-to-carbon ratio favors a much higher Ag weight percent as well as a completely heterogeneous structure on the micro meter scale. It is important for post analysis samples to be well mixed before ascertaining final concentrations [11] [30] [40] [44].

## 5.2. KEMS Experiments

At last, the core results are provided. The first part will include calibration results and associated run numbers that correspond with the experiments. Then, there will be experimental validation provided through the Sr results. Finally, the new work of Ag will be shown to have interesting consequences and discussed more thoroughly in Chapter 6.

### 5.2.1. CALIBRATION RESULTS

**Table 16.** Summary of calibrations performed using Ag in Al<sub>2</sub>O<sub>3</sub> cell. The calibration constant,  $k$ , and temperature differential  $\Delta T$ , *mean* was used to characterize any run after the calibration run, before the next one.

Summary of Ag in Al <sub>2</sub> O <sub>3</sub> Calibration Results							
Run #	$I$ , Melt	% error	T - Melt	$\Delta T$ , Melt	$k$	$\Delta T$ , Hvap	$\Delta T$ , <i>mean</i>
1	$5.45 \times 10^7$	0.19%	1223.67	11.0	$1.333 \times 10^{-32}$	6.1	8.6
2	$1.65 \times 10^7$	0.29%	1228.2	6.1	$4.410 \times 10^{-32}$	5.4	5.7
3	$5.55 \times 10^7$	0.17%	1224.8	9.5	$1.309 \times 10^{-32}$	15.1	12.3
4	$2.24 \times 10^7$	0.25%	1245.9	-11.6	$1.503 \times 10^{-32}$	-19.0	-15.3

Note that the sample run of 2 was significantly better than the rest. Additionally, the temperature differential of calibration runs 3 and 4 were difficult to use; hence, not as much data was obtained using these base experiments. The consistency in the calibration constant, was a boon and ensured that the relation between intensities and pressure across experiments remained intact. This is a key assumption to implement the interpolation through the beta constant.

Throughout the rest of the of the chapter, sample identification shall be recalled back to these calibration results via Table 17. The table also includes the mean associated  $\Delta T$  used to produce results.

**Table 17.** Calibration list for sample number concentration

Sorbed Metal	Sample ID	k ( $10^{-32}$ )	$\Delta T$ (K)	Calib. Run ID
Sr	9	1.50	-15.3	4
	10	1.33	8.3	Pre
	11	1.50	-15.3	4
	13	1.50	-15.3	4
Ag	1		N/A	
	2	1.33	8.6	1
	3		N/A	
	4	1.33	8.6	1
	5	1.50	-15.3	4
	6	1.33	8.6	1
	7	4.41	5.7	2
	8	4.41	5.7	2

Note that the results do not use calibration run three. At this time, some major cleaning needed to be performed on the instrument. The bulk of the Sr validation did occur with a rather large temperature adjustment to the thermocouple, but the statistics of the data points demonstrated consistency, indicating that this calibration run could be used. Also, a preliminary calibration run was performed by the previous user of the KEMS system and served as a referential calibration for sample 10.

### 5.2.2. STRONTIUM

In our analysis, Sr was categorized as a validation step; thus, we tested only a few samples, resulting in a few concentrations tested. No isotherm shall be displayed, since more data would be necessary.

**Table 18.** Data obtained for Sr adsorption to IG-110 graphite. Temperature had an associated uncertainty for temperature, surface concentration and vapor pressure were 0.1 K, < 1%, and < 3%, respectively. The uncertainties in C arise from variance in intensity during a recorded point, and P is the propagation of both I and T uncertainties.

Strontium Data					
Surface Concentration (mmol/kg)	Temperature (K)	Vapor Pressure ( $10^{-9}$ atm)	Surface Concentration (mmol/kg)	Temperature (K)	Vapor Pressure ( $10^{-9}$ atm)
2.92	1548.7	2.588	8.62	1421.7	11.744
3.79	1526.7	2.060	9.59	1353.7	3.610
4.44	1226.0	1.325	9.59	1302.4	8.698
4.91	1287.8	4.978	10.44	1273.7	0.862
5.33	1508.7	1.593	10.62	1263.7	0.814
5.94	1464.5	10.077	11.05	1352.7	5.326
6.08	1456.7	0.507	11.46	1265.6	4.981
6.09	1265.2	3.314	12.67	1287.7	2.425
6.35	1458.7	0.533	13.20	1331.7	7.596
6.55	1334.2	0.907	13.21	1381.7	52.914
6.75	1381.8	2.868	16.02	1296.7	6.531
6.95	1264.5	3.740	18.53	1271.7	5.315
7.05	1377.7	3.174	19.57	1278.7	8.261
7.67	1421.7	9.792	22.06	1299.7	12.222
8.04	1326.1	13.659	24.39	1255.7	8.665

We can then isolate a few data points of strontium for a sample where concentration change is negligible. For these we can develop an enthalpy of vaporization  $\Delta H_{Sr,IG110}$ .

**Table 19.** Enthalpies of vaporization for Sr on IG-110 as measured by KEMS.

Enthalpies of Vaporization for Sr and IG-110 Graphite		
Concentration (mmol/kg)	Average T (K)	$\Delta H_{Sr,IG110}$ (kJ/mol)
11.42 ± 0.81	1331.9	302.2 ± 16.6
5.92 ± 0.15	1474.7	401.4 ± 7.6
10.70 ± 0.26	1301.4	311.2 ± 12.9
7.00 ± 0.73	1378.9	399.4 ± 15.0

Note concentration and temperature do play a role in enthalpy of vaporization, and this becomes more apparent in silver data.

**Table 20.** Hilpert et al.'s experiments on A3-3 graphite, enthalpies of vaporization for strontium [22].

Enthalpies of Vaporization for Sr and IG-110 Graphite		
Concentration (mmol/kg)	Average T (K)	$\Delta H_{Sr,IG110}$ (kJ/mol)
22.3	1147	274.5
13.1	1234	303.8
13.2	1245	297.9
27.1	1255	235.2
6.93	1371	327.6
7.39	1372	323.0
4.00	1378	358.7
3.31	1387	365.4
5.51	1395	331.9
3.62	1416	343.9
2.34	1455	353.6

The enthalpy values roughly agree with the data of Hilpert et al. shown above. For instance, the 311 kJ/mol at 10.7 mmol/kg is similar to the two values of 303.8 and 297.9 kJ/mol at 13.1 and 13.2 mmol/kg, respectively [22]. Some disagreement is expected given the different types of graphite tested and temperature range. We conclude this comparison validated the methodology of our experimental procedure. More data is presented for Myers and Bell presented in Appendix 3 on H-327 graphite [17]. Note this data was unable to be modified from its original image form as the units are in American standard units of kcal/mole.

### 5.2.3. SILVER

Experiments performed on Ag produced successful temperature, surface concentration, and vapor pressure data for Sr. Data for many more samples other than Sr were also used. Full results of tests for silver are presented below, which include higher concentrations as well as lower concentrations.

**Table 21.** Full table of data for silver IG-110 data. The following data had associated uncertainties in C, T, and P. The maximum values for these are 0.1 K for T, 0.85% for C, and 2.6% for P, although more than 63.9% of the points had less than 0.1% uncertainty for C and 0.5% for P. The higher concentrations and temperatures had more uncertainty due to difficulty of stabilizing the equilibrium while comparing to a higher mass loss rate.

Silver Data					
Surface Concentration (mmol/kg)	Temperature (K)	Vapor Pressure ( $10^{-9}$ atm)	Surface Concentration (mmol/kg)	Temperature (K)	Vapor Pressure ( $10^{-9}$ atm)
1.80	1119.9	6.47	20.65	1200.3	53.35
2.09	1167.2	29.46	22.03	1259.8	427.05
2.88	1222.4	135.34	22.26	1199.4	53.58
3.61	1173.5	48.01	23.72	1181.7	152.35
3.65	1244.5	267.57	27.26	1207.0	132.04
4.33	1199.5	103.87	28.14	1174.4	32.75
5.43	1135.8	18.31	28.68	1174.6	33.37
5.56	1257.7	426.97	29.52	1108.0	6.82
5.69	1134.2	17.46	32.90	1205.6	135.89
6.98	1232.7	285.48	36.87	1190.0	103.28
7.17	1227.4	184.54	90.69	1342.5	1434.91
8.01	1156.9	48.57	426.20	1132.9	60.78
8.52	1201.5	158.10	433.79	1186.8	241.14
9.36	1184.4	113.89	455.71	1160.9	140.35
9.79	1181.0	63.41	460.49	1145.4	95.37
10.04	1215.5	254.72	472.34	1200.7	385.49
10.21	1227.4	259.16	485.50	1203.2	422.33
11.36	1172.5	50.32	531.99	1159.6	166.04
12.57	1233.0	313.10	539.87	1132.2	86.69
16.44	1173.6	26.68	744.66	1096.4	63.70
16.87	1253.3	359.26	748.46	1122.2	138.72
17.20	1119.3	24.43	771.79	1209.7	1336.22
17.63	1139.4	41.75	848.74	1142.0	276.05
18.76	1215.3	269.57	873.12	1186.9	923.05
18.78	1222.9	87.74	953.41	1130.3	247.81

We used the low concentrations only in the isotherm plots, as there were not enough data between the low and high concentrations to provide reliable transition. Moreover, the low concentration data are also the most relevant for source term estimations.

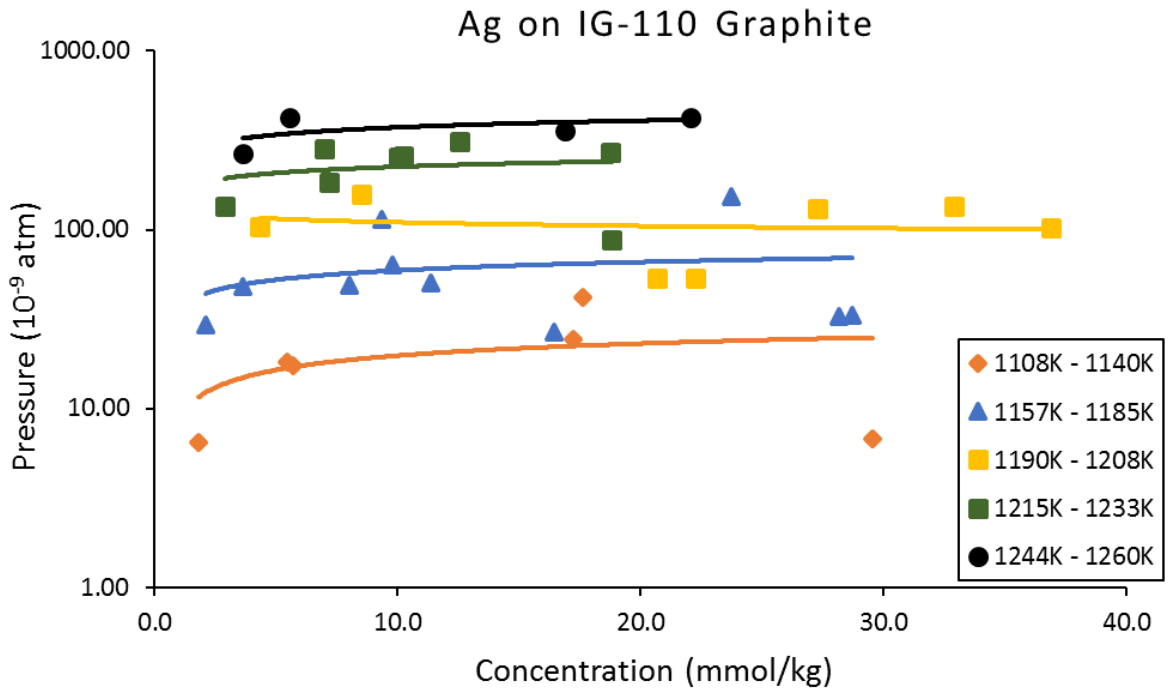


**Figure 28.** The Ag–IG-110 isotherms given by temperature ranges from 1100 K to 1260 K. All data was taken at settings of 70 eV and 2 mA for the electron beam ionization, and a  $10^8$  gain and 1100 V are shown for the detector. The lines represent best fit lines for each set of points. The data also include outliers.

The graph visualizes interesting characteristics. The isotherm shape on a logarithmic graph appears slightly sloped, indicating our data is in the Henrian regime given we have a nearly logarithmic curve. While there are some uncertainties in our results due to estimates of solid phase concentrations of Ag on IG-110, the results fit the expected

form. Using the Excel tool “trendline,” resulted in the isotherm plot in Figure 28. Table 22 reports enthalpies of vaporization, and this data assists in modeling of the source term.

**Table 22.** Enthalpies of vaporization for Ag on IG-110 as performed at NASA GRC.

<b>Enthalpies of vaporization for Ag and IG-110 Graphite</b>		
<b>Concentration (mmol/kg)</b>	<b>Average T (K)</b>	<b><math>\Delta H_{Ag,IG110}</math> (kJ/mol)</b>
2.5 ± 0.3	1177.2	346.1 ± 1.0
4.1 ± 0.3	1213.3	307.2 ± 17.6
7.0 ± 0.5	1170.0	294.0 ± 5.3
8.6 ± 0.3	1198.2	286.4 ± 13.5
17.9 ± 0.2	1158.0	282.9 ± 0.4
23.5 ± 1.3	1179.0	249.7 ± 9.2
24.8 ± 1.7	1231.0	269.5 ± 9.0
468.5 ± 3.3	1178.0	293.8 ± 4.6
755.0 ± 3.7	1142.8	295.3 ± 3.2

Uncertainties in the data shown in Table 21 and Figure 28 relate to the number of measurements associated with a particular concentration and temperature variations. Full description is provided in the discussion section. Variability in concentration is due to significant temperature variation for the run, but more temperature measurements narrow the uncertainty in enthalpy. The data results and methods for Ag are consistent with other fission products.

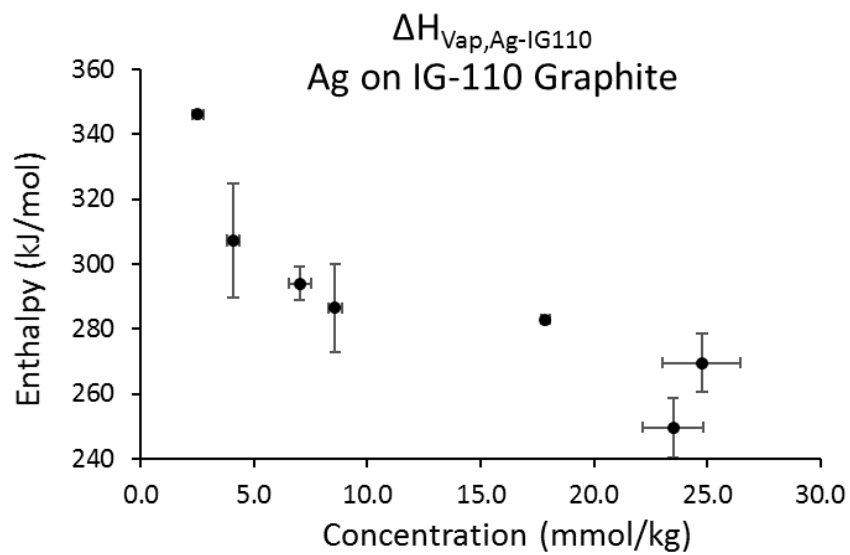


**Figure 29.** Enthalpy of vaporizations for Ag in IG-110 graphite by concentration. Uncertainties, error bars, are shown as percent relations to quantities with roughly 10% for concentration and 3% for enthalpies.

## CHAPTER 6. DISCUSSION AND FUTURE WORK

### 6.1. Discussion of Data Quality

Since we have described the data and the results, it is appropriate to proceed to discussion of inherent uncertainties in this experiment. As noted in Table 10, the data is effectively a stream of intensity unit measurement, which is an averaged property of internal detector reception. The recorded value then marks one measurement that needs to achieve pseudo-equilibrium. For any measurement, the inherent statistical uncertainty can be calculated via a standard deviation. As noted, in Chapter 4, Section 4.2, this factor isn't allowed to rise above 2% for a data point to be considered valid.

Additionally, we have background intensity counts inherent to all mass spectrometers. This is an experimental error, as opposed to an uncertainty, and is quantified in Appendix 2b. The experimental error appears to be three orders of magnitude below most measurements, with a limit of around 5000 counts from shutter closed data obtained at low temperatures. Note this enforced a pressure sensitivity limit dependent on temperature, using the mass spectrometer Eq. 17. Given most  $k$  values were  $1.33 \times 10^{-32}$ ,  $\sigma$  for Ag is  $4.58 \times 10^{-16}$ , and temperatures ranged between 1100 and 1400, a pressure sensitivity limit was necessary, which ranged between  $3.2$  and  $4.0 \times 10^{-10}$  atmospheres [11, 38]. The phenomena was directly observed in the 'burn off' experiments that went awry, as seen in Ag samples 1 and 3.

The temperature error, associated with the thermocouple was accounted for via the calibrations. Temperature uncertainty beyond the calibrated error was the thermocouple reading. This was taken as roughly 0.2 K per temperature reading. Note temperature

ranges were between 1000 and 1400 K, so this uncertainty was roughly 0.014% of the point.

Finally, initial and final concentration data were taken via INAA, which relies on counting rates of neutron-induced radioactivity of metal in the graphite powder. There were two underlying uncertainties in this process. The first was the counting statistics, which were diligently watched to keep below 0.01% of the observed radioactivity. The second uncertainty was uniformity within sample powders. This was addressed and discussed in Table 9, and was found to be roughly 1.09%. This was the largest uncertainty for this process.

In the experiment, there were two primary calculated values reported, concentration, temperature, and pressure (CTP) points as well as enthalpy of vaporization,  $\Delta H_{M-IG110}$ .

CTP points errors arise from the phenomena described. Pressure is synonymous with intensity measurements, given Eq. 17 and temperature measurements were explicitly described. Concentration, had unique handling as it had factored in interpolation between measured quantities and integration of temperature and intensity. The integration effects were proportional to intensity and the square root of temperature. Intensities had a relative uncertainty between 0.1% and 2%, which exceeds the temperature uncertainty of 0.02%; thus, it was taken as the dominating uncertainty. Since the process of measurement is linear and involves interpolation, the effects of uncertainty were additive. Thus, concentration measurements have an uncertainty between 1.1 and 3%.

Enthalpy of vaporization measurements involve regression, and thus the regression statistics were weighed against the collective uncertainty from all the intensity uncertainty from 4 to 8 points. The compiled intensity uncertainty of these points would

have an upper limit of 4% for all data. The tables showing the enthalpy of vaporization factor also revealed an uncertainty with the regression statistics, which outweighed the intensity uncertainty in all cases.

## 6.2. Silver Isotherm Fit

We have reported concentration-temperature-pressure (CTP) data and enthalpy of vaporization,  $\Delta H_{M-IG110}$ . Our CTP data was recorded in mmol/kg, atm, and K. For applications, it would be useful to have a fit to the data of isotherms. Based on the literature, Hilpert et al [22, 23, 24], Myers and Bell [17, 18], and Miller and Armatys [27], we have attempted to fit our data with the form [37]:

$$\ln P_H = \left(A + \frac{B}{T}\right) + \left(X - 1 + \frac{Y}{T}\right) (d_1 - d_2 T) + \ln C_s \quad (33)$$

It is important to note that we performed the substitution for the transition concentration,  $C_t$ . We use A, B, X, Y,  $d_1$ , and  $d_2$  as adjustable constants. Through a first approximation, we arrived with the following results.

**Table 23.** Results of initial fit to Eq. 33.

<b>A</b>	<b>B</b>	<b>X</b>	<b>Y</b>	<b>d<sub>1</sub></b>	<b>d<sub>2</sub></b>
-4.59	0.991	0.996	6.59	0.903	6.67

Note that the transition concentration is effectively the second change in curvature for a Type II isotherm. Plugging in the substituted values based on Eq. 7, for a rough temperature of 1200 K, the initial resulting transition concentration was negative, which gave an irrational finding.

To improve our fit, we bounded the values of constants to ranges based on tables 4-6. And through iteration we, eventually fixed the constants of B, Y, and  $d_2$ , and arrived the following results.

**Table 24.** Results of fit to Eq. 33, but with the fixing of some constants (con).

<b>A</b>	<b>B-con</b>	<b>X</b>	<b>Y-con</b>	<b>d<sub>1</sub></b>	<b>d<sub>2-con</sub></b>
-4.59	-1.54 x 10 <sup>3</sup>	-31.6	7.88 x 10 <sup>3</sup>	6.65	1.88 x 10 <sup>-3</sup>

The resulting  $C_t$  for this fit was 81.2 mmol/kg, which seems reasonable given a visual analysis of data for high and low concentrations in Appendix 4. The results vary widely from the two fits, but the resulting transition concentration yields some confidence. Moreover, the regression error reduced significantly, although that might be a consequence of reducing the fitting constants from 5 to 3.

Theory and form indicate that CTP data is interrelated. Although there does not seem to be a full integrated dependence on T with  $C_s$ . So, we decided to create a new form to fit the parameters that explicitly had multi ordered dependence on temperature.

$$\ln P = \left( A + \frac{B}{T} + d_1 T \right) + \left( X + \frac{Y}{T} + d_2 T \right) \ln C_s \quad (34)$$

**Table 25.** Results of fit to Eq. 34

<b>A</b>	<b>B</b>	<b>d<sub>1</sub></b>	<b>X</b>	<b>Y</b>	<b>d<sub>2</sub></b>
-52.9	0.909	3.06 x 10 <sup>-2</sup>	2.57	1.01	-2.12 x 10 <sup>-3</sup>

The best regression came from this fit, although relating it back to current theory is still a work in progress. Much work needs to still be done in this area, as the regression function did not converge so the resulting error is distributed as uncertainty among the actors.

### 6.3. Importance of Data

We obtained experimental sorption and enthalpy of vaporization data for Sr and Ag on IG-110 graphite. Images using SEM provide some visual insights into the bonding and possible mechanisms during the KEMS experiment. EDS was used in support of the SEM imaging to clarify atomic compositions. This led to possible oxidation during sample processing, but demonstrated that it was likely sorbed water. Most of the post sample analysis demonstrated negligible oxygen. Given the “burn off” step, the mechanism captured is strictly fission product sorption on graphite.

Strontium data shown in Table 19, though limited, agreed with previous data of Hilpert et al, Table 20, and Myers & Bell, Appendix 3. The comparable data is within the margin of error, and provides validation for the experiment and methods. The major bonding characteristics and subsequent enthalpies of vaporization data of our experiments remain similar for Sr throughout the various graphite, as compared to work done by Hilpert et al [22] and Myers and Bell [17].

Previous experiments used radioactive samples to measure surface concentration. In this experiment, non-radioactive sorbate was required, so an interpolation technique was used. Mass loss was observed to have significant effects, especially at higher temperature measurements of vapor pressure. The ‘burn off’ procedure provided some effect and further ensured a uniform sample. It also caused variance in the count rates over time. Our data noted larger statistical deviations at higher concentrations and temperatures. This was a consequence of the method, which started with final concentration measurements and the interpolation reverted to the initial concentration. This does inherently propagate statistical uncertainty towards the higher concentrations. Despite

possible uncertainties the developed interpolation method provided uniformity throughout experimental data. This was shown through the calculated Sr data, and validates that the observed mass loss was compensated by the interpolation method.

Ag data as shown in Figure 28 was consistent with the expected isotherm curvature. This data is the first Ag sorption on graphite experimental data. The imaging analysis and EDS performed yield insights into the binding of Ag and graphite. Comparing before and after images, Ag tends to cluster. Reviewing the theoretical work of Wang and Duffy, who used PLATO to find binding energies, we find that they underestimated binding strength. The qualitative aspects of Figure 26, indicates faceted localized silver. Additionally, comparing Figures 24 and 25, there is significant drive for Ag to cluster in the graphite matrix. These two effects yield strong binding energies at low concentrations and is consistent with sorption theory and clearly demonstrated in the graphite of Figure 29.

Comparing the data in tables 18 and 21 and Figure 21, we anticipate that the transition concentration from Langmuir to Henrian isotherms for IG-110 graphite and Ag can be found between concentrations of 36 and 91 mmol/kg. This is one example of future work that could be performed related to fission product sorption on graphite.

#### 6.4. Other Areas of Future Work

Another area pertaining to follow up is understanding the higher statistical deviations at higher concentrations. While our method does propagate, error going up in mass loss data observed at high temperatures was difficult to obtain even at pseudo equilibrium as shown in Figure 11. The ‘burn off’ step did provide controlled concentrations, but depleted some of the sorbed sample, typically reducing control on experimented concentration data. Future work will need to overcome, or through repetition, control this effect.

Although the initial work was performed comparing IG-110 and NBG-18, the two leading candidates for practical TRISO fuel use, other graphitic matrices, soon to be developed or historical candidates such as A3-3, can be tested with this technique. Further the method provided in my research circumnavigates the precautions of handling radioactive material. As such, it expands the base of experimenters to those who have any KEMS instrument. Although, this is a small subset of the experimental community. It will also be of interest to expand the various types of mass analyzers attached to the Knudsen cell, for instance attaching a ICP-MS.

The concentration range of 150 to 30 mmol/kg should be the aim of future Ag experiments. Sorption measurements can be performed for other fission products. Replication studies can also be conducted on other fission product materials such as Cs data on IG-110. Additionally, other graphite types should be investigated to contribute to the understanding of fission product sorption. Research is needed to elucidate the various properties that are important for retention and release of radioisotopes.

Of particular interest is the chemisorption potential for various species, RSA efficiency, diffusion and intercalation efficiency, microstructure effects (grain size, BET, porosity distribution, source material), and at partial pressures of hydrogen (tritium and entrained water) over a range of high temperatures (500–1600 C). The sorption/desorption isotherms of key fission products (including silver, cesium, strontium, and europium) in irradiated nuclear grade graphite for the high temperature reactors need to be determined. Projects should include studies of the effect of irradiation. Further, comparisons should be made of radioactive versus non-radioactive isotopes of the key fission products, which serve as surrogates to determine fission product retention behavior. The comparisons will assist in understanding effects of irradiated TRISO fuel forms [1, 8].

Finally, as noted in the imaging section, oxidization is inevitable with these studies, but is alleviated in the sample preparation technique. Future research should include testing various levels of oxidization, on fission product sorption and retention.

Data from KEMS in conjunction with SEM and EDS analysis typically provides a complete chemical and physical picture of sorption. Additionally, the effects of multiple fission products and a variety of other possible chemical structures would provide insight into the field of fission product sorption. The techniques and methods provided in this thesis have the capabilities to provide insights into these areas.

## References

- [1] Idaho National Lab, "HTGR Mechanistic Source Terms White Paper," U.S. DOE, Idaho Falls, July 2010.
  
- [2] International Atomic Energy Agency, "Fuel performance and fission product behaviour in gas cooled reactors," INIS Clearinghouse, Vienna, Austria, 1997.
  
- [3] U.S. Nuclear Regulatory Agency, "*NRC Regulations Title 10, Code of Federal Regulations*", North Bethesda: U.S. Government Printing Office, 2017.
  
- [4] K. Walton, T. Ghosh, D. Viswanath, S. Loyalka and R. Tompson, "Adsorption of iodine on graphite in High Temperature Gas-Cooled Reactor systems: A review," *Progress in Nuclear Energy*, no. 73, pp. 21-50, 2014.
  
- [5] World Nuclear Association, "Advanced Nuclear Power Reactors," January 2017. [Online]. Available: <http://www.world-nuclear.org/information-library/nuclear-fuel-cycle/nuclear-power-reactors/advanced-nuclear-power-reactors.aspx>. [Accessed April 2017].
  
- [6] Hahn-Meitner-Institut, "Transport of Fission Products in Matrix and Graphite," Berlin, 1983.
  
- [7] J. Lee, T. Ghosh and S. Loyalka, "Oxidization rate of nuclear-grade graphite NBG-18 in the kinetic regime for VHTR air ingress accident scenarios," *Journal of Nuclear Materials*, pp. 77-87, 2013.
  
- [8] T. Burchell, R. Bratton and W. Windes, "NGNP Graphite Selection and Acquisition Strategy," Oak Ridge National Laboratory, Oak Ridge, 2007.
  
- [9] A. Mohan, R. Tompson and S. Loyalka, "Efficient numerical solutions of the Clausen problem," *Journal of Vacuum Science & Technology*, pp. 758-762, 2007.

- [10] A. Booth, T. Markus, G. McFiggans, C. Percival, M. McGillen and D. Topping, "Design and construction of a simple Knudsen Effusion Mass Spectrometer (KEMS) system for vapour pressure measurements of low volatility organics," *Atmospheric Measurement Techniques*, no. 2, pp. 355-361, 2009.
- [11] P. Atkins and J. De Paula, *Atkins' Physical Chemistry*, 8th ed., New York: Oxford New York, 2006.
- [12] Hiden Isochema Ltd, "Hiden Isochema: Advancing Sorption Analysis," Hiden Isochema, 01 April 2015. [Online]. Available: <http://www.hidenisochema.com/>. [Accessed 13 April 2015].
- [13] J. Berg, P. Calderoni, G. Groenewold, P. Humrickhouse and P. Winston, "Single Component Sorption-Desorption Test Experimental Design Approach Discussions," Idaho National Laboratory, Idaho Falls, 2011.
- [14] P. L. J. T. W. Connor, "The adsorption of iodine by graphite," in *Fifth Conference on Carbon*, New York, 1961.
- [15] F. Salzano, "Adsorption of iodine by graphite," New York, 1961.
- [16] F. Salzano, "The behavior of iodine in graphite," *Carbon* 2, New York, 1964.
- [17] B. Myers and W. Bell, *Strontium Transport Data for HTGR Systems*, San Diego: General Atomic Project, 1974.
- [18] B. Myers and W. Bell, "Cesium Transport Data for HTGR Systems," General Atomic Company, San Francisco, 1979.
- [19] K. O. J. Iwamoto, "The behavior of iodine in adsorption and desorption by graphite," vol. 5, no. 9, pp. 437-446, 1968.
- [20] M. C. E. d. N. H. Osborne, "Studies of Iodine Adsorption and Desorption on HTGR Coolant Circuit Materials," Oak Ridge National Lab, Oak Ridge, 1976.

- [21] R. D. F. T. R. Lorenz, "Sorption/desorption Behavior of Iodine on Graphite," Oak Ridge National Lab, Oak Ridge, 1982.
- [22] K. Hilpert, H. Gerads and D. Kobertz, "Sorption of Strontium on Graphitic Materials," *Berichte Der Bunsen-Gesellschaft*, vol. 89, no. 1, pp. 43-48, January 1985.
- [23] K. Hilpert, "Potential of mass spectrometry for the analysis of inorganic high-temperature vapors," *Fresenius Journal of Analytical Chemistry*, no. 370, pp. 471-478, 2001.
- [24] K. Hilpert, H. Gerads, D. Kath and D. Koberts, "Sorption of Cesium and its vaporization from graphitic materials at high temperatures," *High Temperatures - High Pressures*, vol. 20, pp. 157-164, 1988.
- [25] E. Copland and N. Jacobson, "Measuring Thermodynamic Properties of Metals and Alloys with Knudsen Effusion Mass Spectrometry," NASA Center for Aerospace Information, Hanover, 2010.
- [26] J. Colle, O. Benes and R. Konigs, "Knudsen Effusion Mass Spectrometry of Nuclear Materials: Applications and Developments," *ECS: Transactions*, vol. 1, no. 46, pp. 23-38, 2013.
- [27] M. Miller and K. Armatys, "Twenty Years of Knudsen Effusion Mass Spectrometry: Studies Performed in the Period of 1990-2010," *The Open Thermodynamics Journal*, no. 7, pp. 2-9, 2013.
- [28] E. Copland and N. Jacobson, "Thermodynamic Activity Measurements with Knudsen Cell Mass Spectrometry," *ECS: Interface*, no. Summer, pp. 28-31, 2001.
- [29] S. Branney, "The Adsorption of Fission Products on VHTR Structural Materials," University of Missouri, Columbia, 2010.
- [30] J. Drowart, C. Chatillon, J. Hastie and D. Bonnell, "High-Temperature Mass Spectrometry: Instrumental Techniques, Ionization Cross-Sections, Pressure Measurements, and Thermodynamic Data," *Pure Applied Chemistry*, vol. 77, no. 4, pp. 683-737, 2005.
- [31] Merriam-Webster, "Isopiestic," 2017. [Online]. Available: <https://www.merriam-webster.com/dictionary/isopiestic>. [Accessed 25 04 2017].

- [32] A. Londono-Hurtado, L. Szlufarska, R. Bratton and M. D., "A review of fission product sorption in carbon structures," *Journal of Nuclear Materials*, no. 426, pp. 254-267, 2012.
- [33] I. Szlufarska, "Modeling Fission Product Sorption in Graphite Structures," Madison, 2013.
- [34] G. Wang, J. BelBruno, S. Kenny and R. Smith, "Interaction of silver adatoms and dimers with graphite surfaces," *Surface Science*, no. 541, pp. 91-100, 2003.
- [35] M. Greenlief, *Vapor Pressure of a Solid by Knudsen Effusion*, Columbia, Missouri: Mizzou Publishing, 2016.
- [36] E. Hoffmann and V. Stroobant, *Mass Spectrometry: Principles and Applications*, West Sussex: John Wiley & Sons, Ltd, 2007.
- [37] A. Shilov, L. Holappa and V. Stolyarova, "A Knudsen Effusion High Temperature Assembly for a Quadrupole QMG-420 Mass Spectrometer," *Rapid Communications in Mass Spectrometry*, vol. 11, pp. 1425-1429, 1997.
- [38] ThermoFinnigan, MAT 253: Operating Manual, Bremen: ThermoFinnigan, 2002.
- [39] G. Goldstein, D. Newbury, P. Echlin, D. Joy, C. Fiori and E. Lifshin, *Scanning Electron Microscope and X-ray Microanalysis*, New York: Plenum Press, 1981.
- [40] G. Costa, J. McDonough, Y. Gogotsi and A. Navrotsky, "Thermochemistry of onion-like carbons," *ELSEVIER: Carbon*, no. 69, pp. 490-494, 2014.
- [41] D. D. Wagman, W. Evans, I. Halow, V. Parker, S. Bailey and R. Schumm, *Selected Values of the Thermodynamic Properties of the Elements*, Metals Park: American Society for Metals, 1973.
- [42] J. Ferraro and K. Krishnan, *Practical Fourier Transform Infrared Spectroscopy*, San Diego: Academic Press Limited, 1990.

- [43] J. Coates, "Interpretation of Infrared Spectra, A Practical Approach," in *Encyclopedia of Analytical Chemistry*, Chichester, John Wiley & Sons Ltd, 2000, pp. 10815-10837.
- [44] Royal Society of Chemistry 2014, "'Cesium' 'Strontium'," 31 October 2014. [Online]. Available: <http://www.rsc.org/periodic-table/>.
- [45] P. Harris, "New Perspectives on the Structure of Graphite Carbons," *Solid State and Materials Sciences*, no. 30, pp. 235-253, 2005.

## Appendix 1: Additional Reference Theory

### A) EQUILIBRIUM CONSTANT RELATION

For a basic reaction



Has an equilibrium constant of  $K_p = p_A$  and similarly  $K_p = p_B$  for the following reaction



Of particular interest, though, is the full disassociation reaction



with equilibrium constant being related to

$$K_p = \frac{p_A p_B}{p_{AB}} \quad (\text{A1.4})$$

which is very commonly studied. According to the second and third law methods a general enthalpy of reaction can be related to the equilibrium constant:

$$\Delta H_T^0 = \frac{d \ln K_p}{d(1/T)} \quad (\text{A1.5})$$

### B) THERMODYNAMIC GENERALIZATION

Recall the Freundlich isotherm

$$\ln p = \left( A + \frac{B}{T} \right) + \left( D + \frac{E}{T} \right) \ln C_g \quad (\text{A1.6})$$

Thus, enthalpy of vaporization follows, and  $\Delta H$ , is linearly independent of  $\ln C$

$$\Delta H = -R \frac{\partial \ln p}{\partial (1/T)} = -R \left( B + E \ln C_g \right) \quad (\text{A1.7})$$

There is a concentration in which one has a regime change of transportation for low concentrations referenced as  $C_T$ , which is when the desorption species exhibits Henrian behavior; thus, the Henrian isotherm is

$$\ln p = \left(A + \frac{B}{T}\right) + \left(D - 1 + \frac{E}{T}\right) \ln C_T + \ln C_g \quad (\text{A1.8})$$

Typically,  $C_T$  or  $\ln C_T$  can be indicated as a constant or a scaling factor relating to temperature,  $T$ .

### C) NEUTRON ACTIVATION ANALYSIS (NAA)

Neutron activation analysis (NAA) is used to determine the concentration in graphite powder before and after operation. The basic premise is that elements in a sample are exposed to neutrons and then form radioactive isotopes, which decay. The spectrum, typically gamma rays  $\gamma$ , are studied to determine the activity and thus initial concentration. The relevant activation equation is:

$$C = \sigma\varphi N_T (1 - e^{-\lambda t, irr}) e^{-\lambda t, d} \quad (\text{A1.9})$$

In this equation,  $C$  is the activity after irradiation in decays per second (Bq),  $\sigma$  is the neutron cross section of the material, and  $\varphi$  is the neutron flux of the exposure. Also,  $N_T$  is the number of atoms in the target and  $\lambda$  is the decay constant of the radioisotope studied. These are impacted by the irradiation (irr) and decay (d) times.

Typical use of this analysis is to perform comparative analysis. One starts with a standard (std) of mass for the element being studied for each group of irradiations and then calculates  $N_T$  of the sample (sm) directly by comparing activity.

$$\frac{N_{SM}}{N_{STD}} = \frac{C_{SM} \lambda \Delta t_c / (1 - e^{-\lambda t, irr}) e^{-\lambda t, d}]_{SM}}{C_{STD} \lambda \Delta t_c / (1 - e^{-\lambda t, irr}) e^{-\lambda t, d}]_{STD}} \quad (\text{A1.10})$$

This equation is simply solving for mass of sample, where  $C_i$  is the counts measured of ( $i$ ); The count time,  $\Delta t_c$ , time of irradiation and decay time are all meant to be constant across studies, but variances can occur; thus, these variances are accounted for in the bracket notation given.

Also note,  $\lambda$  can be reduced, but it is common to perform multiple standards and create a regression line based on multiple  $C_{STD}$ . In this case, the entire denominator is substituted by this regression slope, and in this case, the decay constant should be maintained in the numerator.

#### D) MASS-WEIGHT CALIBRATION

This can be followed for either Sr or Ag and thus the subscript is dropped [11].

$M$  is molecular weight,  $m$  is mass, with subscripts 'b' for metal before the experiment, 'a' for metal after the experiment, and IG110 for powder mass;  $w$  is weight of the sample, and  $c$  is molar concentration following the same subscript rules;

$$m_b = w \cdot c_b \cdot M \quad (A1.11)$$

Mass of metal is initially calculated from the weight and weight is represented by sum of metal and powder

$$w = m_b + m_{IG110} \quad \text{or} \quad m_{IG110} = w - m_b \quad (A1.12a,b)$$

Concentration after operation comes from measured data; thus, we need to derive the mass after operation.

$$c_a = \frac{m_a}{(m_a + m_{IG110}) \cdot M} \quad (A1.13)$$

$$m_a = \frac{M \cdot c_a \cdot m_{IG110}}{(1 - M \cdot c_a)} \quad (A1.14)$$

## Appendix 2: Supplemental Raw Data

### A) KEMS RAW DATA SAMPLES

Thermocouple data is observed in conjunction with ionization data.

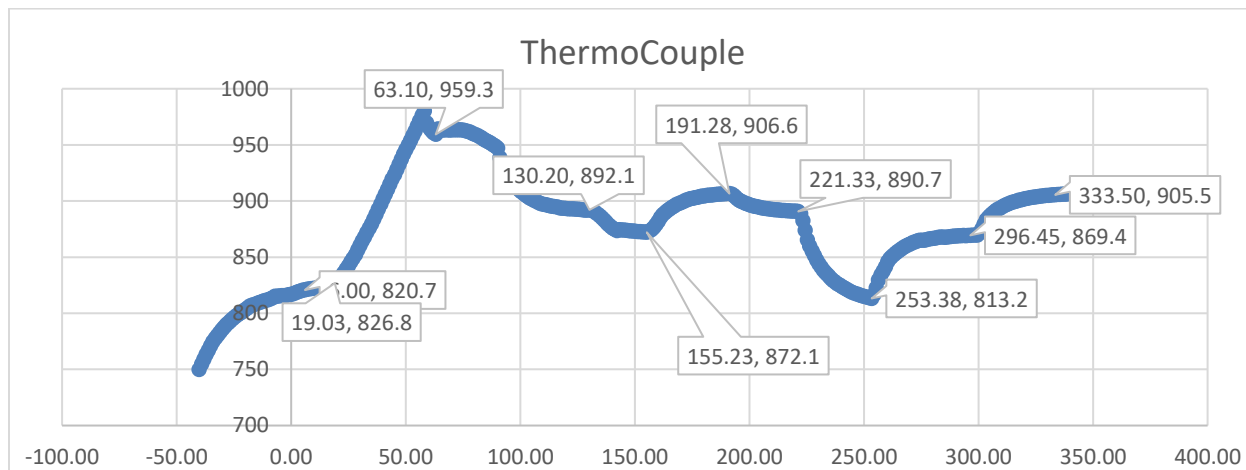


**Figure A2.1** The thermocouple reading for a Ag calibration sample experiment. The equilibrium points are matched via time measurements with those in the ionization data.

### B) SHUTTER EXPERIMENTS

The associated intensity data for Figure A2.1 is provided in Figure A2.2. This intensity data though is meant to highlight the observed significant of data points. The apparatus has a shutter, which can be open and closed. The drop offs are three-minute closings of the shutter. While, background might have risen with respect to temperature, the observed data points remain well above background.

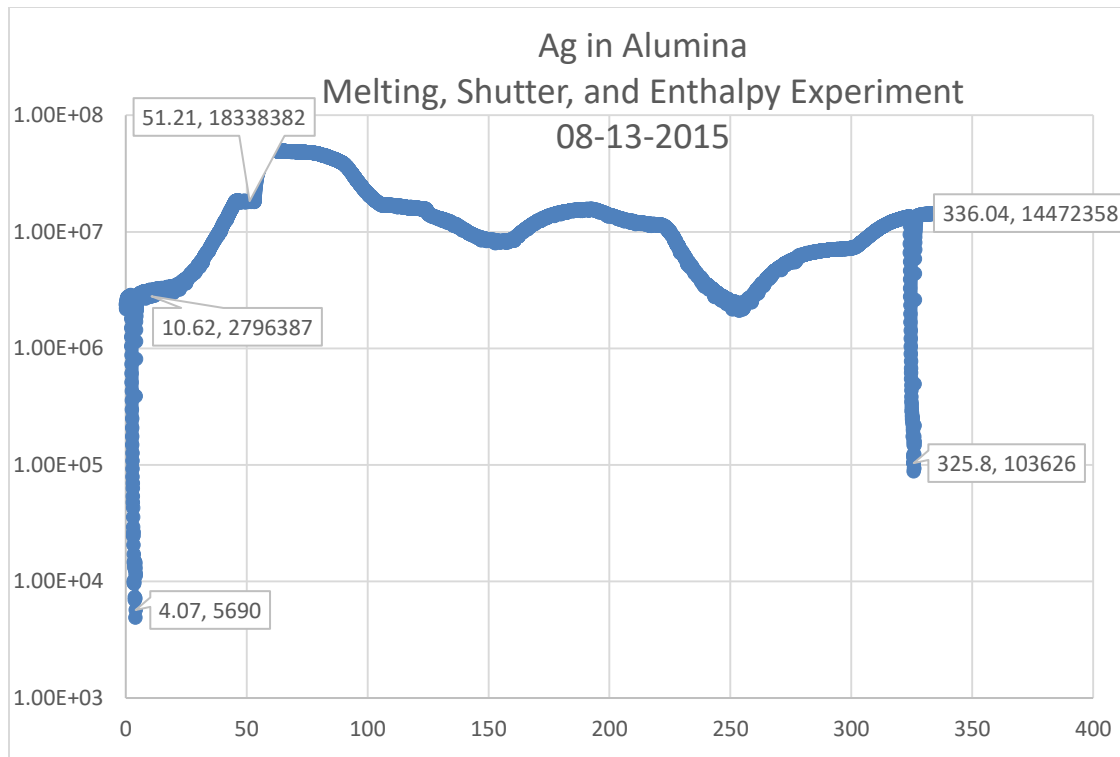


**Figure A2.2** Ag in Alumina calibration experiment. This figure shows, on a logarithmic scale, that uncertainty in intensity units is nearly a fixed fractional percentage. As a result, the background is statistically insignificant.

### C) RAW DATA OF FIRST POINT

Data is identified through comparing intensity and temperature points. As part of the comprehensive experiments, preliminary data was performed with Sr on IG-110.

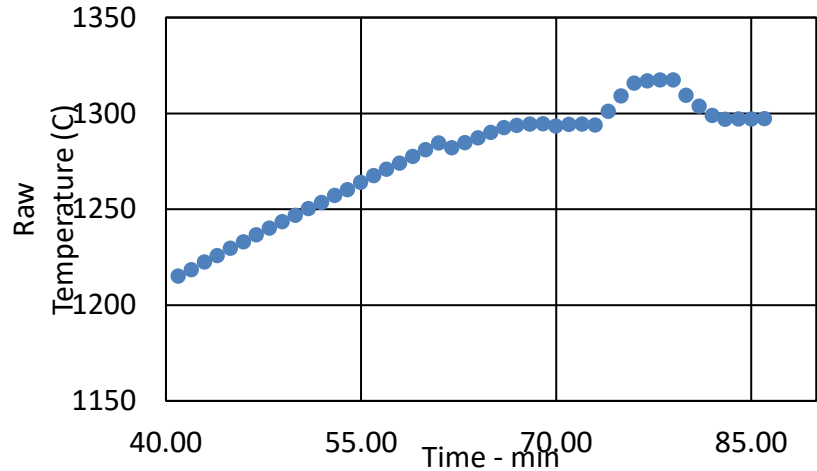


**Figure A2.3** Thermocouple reading graph for preliminary Sr on IG-110 graphite experiment.

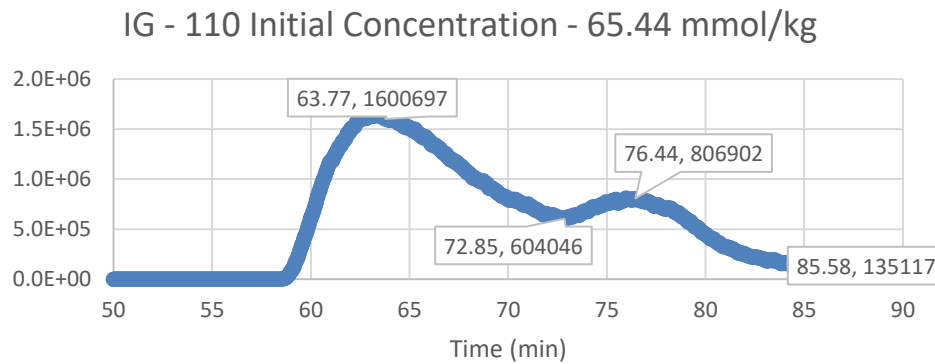


**Figure A2.4** Continuing the analysis from Figure A2.3, this graph shows how pseudoequilibrium can be achieved.

We noted that while we wished to focus on key temperature ranges, significant reduction in counts is observed at high temperatures over long time. Mass loss rate is significant, and sample is relatively exhausted at only the 85-minute mark. However, this experimentation ensured that KEMS was the proper instrument to obtain fission product sorption data.

### Appendix 3: Supplemental Data of Previous Work

**Table A3.1** Review of experimental and modeled binding energy or enthalpy of vaporization of fission product sorbate to designated surface material, or bonding location on a graphene sheet. Experiment (Exp) is further categorized by the concentration. Further, the fission product mean temperature of the experiment or model is listed, if it is relevant information [34].

Fission Product	Material	Author	Energy	Units	Energy in kJ/mol	Exp or Model Used
Ag	$\alpha$ spot	Wang,	0.43	eV/atom	41.43	PLATO, adatom func.
Ag	$\beta$ spot	Wang	0.439	eV/atom	42.30	PLATO, adatom func.
Ag	Over Bond	Wang	0.434	eV/atom	41.82	PLATO, adatom func.
Ag	Over Hole	Wang	0.392	eV/atom	37.77	PLATO, adatom func.
Ag	$\alpha$ spot	Duffy	0.27	eV/atom	26.02	PLATO, adatom func.
Ag	$\beta$ spot	Duffy	0.54	eV/atom	52.03	PLATO, adatom func.
Ag	Over Bond	Duffy	0.23	eV/atom	22.16	PLATO, adatom func.
Ag	Over Hole	Duffy	0.33	eV/atom	31.80	PLATO, adatom func.
Ag	$\alpha$ spot	Wang	2.993	eV/atom	288.38	PLATO, dimer func.
Ag	$\beta$ spot	Wang	2.991	eV/atom	288.19	PLATO, dimer func.
Ag	Bond	Wang	3.003	eV/atom	289.35	PLATO, dimer func.
Ag	Bond	Wang	2.983	eV/atom	287.42	PLATO, dimer func.
Ag	Hole A	Wang	3.032	eV/atom	292.14	PLATO, dimer func.
Ag	Hole B	Wang	3.023	eV/atom	291.27	PLATO, dimer func.
Ag	$\beta$ 2 spot	Wang	3.008	eV/atom	289.83	PLATO, dimer func.
Cs (0K)	H-327	Scrufalska	2.3	eV/atom	221.61	VASP
	H-451					
Cs (0K)	Unirrad	Scrufalska	2.01	eV/atom	193.67	VASP
Cs (0K)	H-451 Irrad	Scrufalska	1.41	eV/atom	135.86	VASP
	Fuel Rod					
Cs (0K)	Matrix	Scrufalska	2.81	eV/atom	270.75	VASP
Cs (1035K)	A3-3	Hilpert	237	kJ/mol	237.00	Exp (34.8 mmol/kg)
Cs (1166K)	A3-3	Hilpert	259	kJ/mol	259.00	Exp (21.1 mmol/kg)
Cs (1253K)	A3-3	Hilpert	295	kJ/mol	295.00	Exp (4.22 mmol/kg)
Cs (1373K)	H-327	Scrufalska	2.92	eV/atom	281.35	VASP
	H-451					
Cs (1373K)	Unirrad	Scrufalska	3.3	eV/atom	317.96	VASP
Cs (1373K)	H-451 Irrad	Scrufalska	3.65	eV/atom	351.68	VASP
	Fuel Rod					
Cs (1373K)	Matrix	Scrufalska	3.12	eV/atom	300.62	VASP
Cs (973K)	H-327	Scrufalska	2.74	eV/atom	264.00	VASP
	H-451					
Cs (973K)	Unirrad	Scrufalska	2.92	eV/atom	281.35	VASP
Cs (973K)	H-451 Irrad	Scrufalska	3	eV/atom	289.06	VASP

Cs (973K)	Fuel Rod Matrix	Scrufalska	3.03	eV/atom	291.95	VASP
Sr	H-327 Fuel Rod Matrix	Scrufalska	4.491	eV/atom	432.72	VASP
Sr	Matrix	Scrufalska	5.16	eV/atom	497.18	VASP
Sr (1147K)	A3-3	Hilpert	274.5	kJ/mol	274.50	Exp (22.3 mmol/kg)
Sr (1234K)	A3-3	Hilpert	303.8	kJ/mol	303.80	Exp (13.1 mmol/kg)
Sr (1238K)	A3-3	Hilpert	235.6	kJ/mol	235.60	Exp (88.5 mmol/kg)
Sr (1245K)	A3-3	Hilpert	297.9	kJ/mol	297.90	Exp (13.2 mmol/kg)
Sr (1251K)	A3-3	Hilpert	220.2	kJ/mol	220.20	Exp (59.1 mmol/kg)
Sr (1255K)	A3-3	Hilpert	235.2	kJ/mol	235.20	Exp (27.1 mmol/kg)
Sr (1280K)	A3-3	Hilpert	213.5	kJ/mol	213.50	Exp (79.9 mmol/kg)
Sr (1323K)	A3-3	Hilpert	217.3	kJ/mol	217.30	Exp (61.9 mmol/kg)
Sr (1371K)	A3-3	Hilpert	327.6	kJ/mol	327.60	Exp (6.93 mmol/kg)
Sr (1372K)	A3-3	Hilpert	323	kJ/mol	323.00	Exp (7.39 mmol/kg)
Sr (1378K)	A3-3	Hilpert	358.7	kJ/mol	358.70	Exp (4 mmol/kg)
Sr (1387K)	A3-3	Hilpert	365.4	kJ/mol	365.40	Exp (3.31 mmol/kg)
Sr (1395K)	A3-3	Hilpert	331.9	kJ/mol	331.90	Exp (5.51 mmol/kg)
Sr (1416K)	A3-3	Hilpert	343.9	kJ/mol	343.90	Exp (3.62 mmol/kg)
Sr (1455K)	A3-3	Hilpert	353.6	kJ/mol	353.60	Exp (2.34 mmol/kg)
Sr (1659K)	A3-3	Hilpert	447.8	kJ/mol	447.80	Exp (0.342 mmol/kg)
Sr (1786K)	A3-3	Hilpert	467.9	kJ/mol	467.90	Exp (0.176 mmol/kg)
Sr (1788K)	A3-3	Hilpert	484.3	kJ/mol	484.30	Exp (0.0388 mmol/kg)
	Binder Coke	Scrufalska	2.907	eV/atom	280.10	VASP

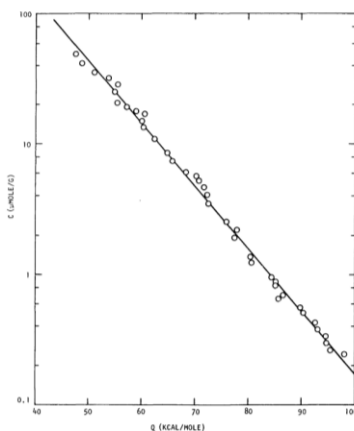


**Figure A3.1.** Myers and Bell, enthalpy of vaporization of Sr on H-273 graphite [17]

## Appendix 4: Isotherm Regression Material

### A) FULL AG DATA

Code for the Mathematica file is available upon request from the Nuclear Science and Engineering Institute or the author.

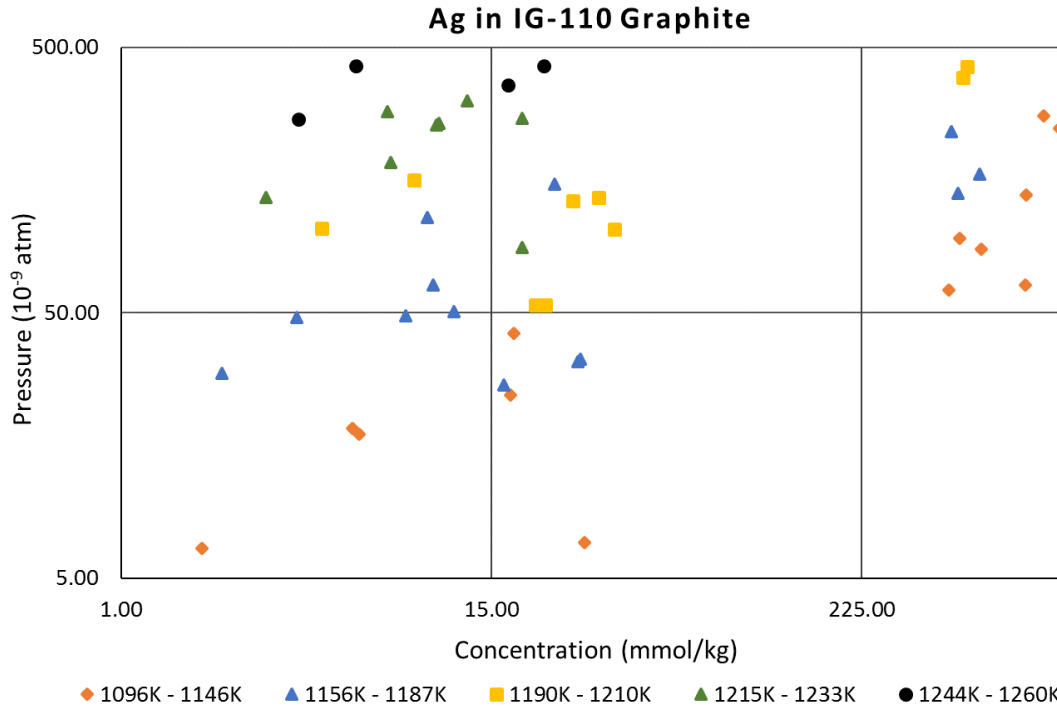


**Figure A4.1.** Ag data including high and low concentration data. The isoform visually fits between roughly 40 mmol/kg and 240 mmol/kg.

## VITA

### **John-David Bernard-Ludwig-Philip Seelig**

6105 Avenida Alteras, Rancho Santa Fe, CA 92067

John-David Bernard-Ludwig-Philip Seelig (JD) was born October 5, 1986, in San Diego California. He enrolled in UC Berkeley with over 40 credits from Advanced Placement Program (AP) classes and received his Bachelors in Science in Chemical Engineering in May 2009, but focused in energy production, materials science, and nuclear engineering.

During two of his summers he interned at Taricco Corporation, an autoclave manufacturing company in Long Beach where he met his first mentor in the field of engineering, Tari Tarricco. He also participated in research one summer at San Diego State University, while taking summer classes. He enrolled in University of California-Berkeley Extension taking graduate level nuclear engineering classes from June 2009 until May 2010. During that year he also passed the Field Engineer Exam for the State of California in chemical engineering. He obtained his MS in nuclear engineering from University of Missouri in July, 2012. He began pursuing the work that led to this dissertation at the University of Missouri-Columbia in June, 2014, continuing research introduced to him by colleagues and peer mentors Mike Reinig and Matt Simones.

His PhD project encouraged collaboration between many different groups, NSEI, MURR, NASA-GRC, and the MU College of Engineering. JD helped build the MU College of Engineering Freshmen Enrichment Program, under the direction of Jill Ford, then Tina Balser, then Nick Balser. Additionally, he also took classes in Finance. He became a founding member of the University of Missouri Investment Group, an equity-based student group. Additionally, he

helped Ryan Wenk, Kyle Cleeton, and Ray Troy found the Student Angel Capital Program. Under the tutelage and supervision of Professor W.D. Allen, the group raised over \$600,000 to establish an evergreen fund. It was renamed in 2015, the Allen Angel Capital Education Fund, and has become a key investor in six projects. JD also participated in the MU Investment Fund Program, which extended to the CFA Research Challenge where he earned 2nd place at the local collegiate competition level. He passed the FINRA Exams, Series 65 and 3 during his last year.

In 2016 he helped Dr. Mark Prelas and his peers write a book entitled, Nuclear Batteries and Radioisotopes. He anticipated continuing his research work for DOE and planned to pursue NASA-related interests, but the job opportunities were removed due to initial budget constraints in 2017. He assisted in the proposal writing to ensure his dissertation research project, could be pursued by the next generation of students. In June 2017, he will begin work at Tradebot, a higher frequency equity, futures, and commodities trading company (HFT), in Kansas City, Missouri. He received his PhD in nuclear engineering from the University of Missouri-Columbia in June 2017.